Cell Reports

Article

Microglia colonize the developing brain by clonal expansion of highly proliferative progenitors, following allometric scaling

Graphical abstract

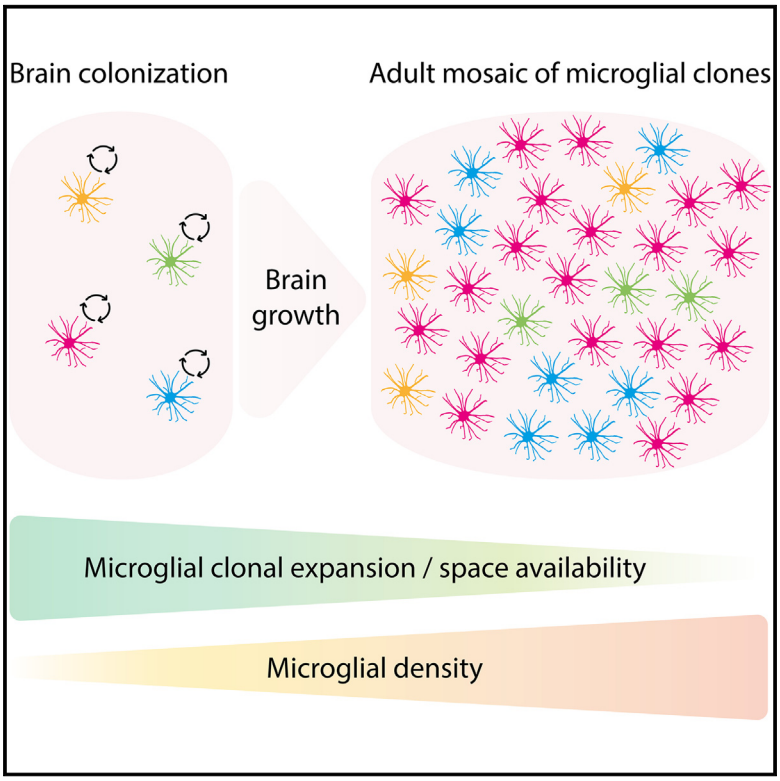

Authors

Liam Barry-Carroll, Philip Greulich, Abigail R. Marshall, ..., Olga Garaschuk, David A. Menassa, Diego Gomez-Nicola

Correspondence

d.gomez-nicola@soton.ac.uk

In brief

Microglia play central roles in brain development, but their precise dynamics are not well understood. Barry-Carroll et al. describe the dynamics of the microglial population during mouse brain development, identifying clonal expansion as a key mechanism determining how microglia colonize the brain and form the adult population.

Highlights

- The microglial population expands proportionally to brain growth, known as allometric scaling
- Microglia expand clonally both during embryonic and postnatal development
- Different microglial clones have distinct expansion capacity, competing for available space

Barry-Carroll et al., 2023, Cell Reports *42*, 112425
May 30, 2023
https://doi.org/10.1016/j.celrep.2023.112425

CellPress

Cell Reports

CellPress
OPEN ACCESS

Article

Microglia colonize the developing brain by clonal expansion of highly proliferative progenitors, following allometric scaling

Liam Barry-Carroll,[1] Philip Greulich,[2,6] Abigail R. Marshall,[1] Kristoffer Riecken,[3] Boris Fehse,[3] Katharine E. Askew,[1] Kaizhen Li,[4] Olga Garaschuk,[4] David A. Menassa,[1,5] and Diego Gomez-Nicola[1,6,7,*]

[1]School of Biological Sciences, University of Southampton, Southampton General Hospital, Southampton, UK
[2]School of Mathematical Sciences, University of Southampton, Southampton, UK
[3]Research Department Cell and Gene Therapy, University Medical Center Hamburg-Eppendorf, Hamburg, Germany
[4]Department of Neurophysiology, University of Tübingen, Tübingen, Germany
[5]The Queen's College, University of Oxford, Oxford, UK
[6]Institute for Life Sciences (IfLS), University of Southampton, Southampton, UK
[7]Lead contact
*Correspondence: d.gomez-nicola@soton.ac.uk
https://doi.org/10.1016/j.celrep.2023.112425

SUMMARY

Microglia arise from the yolk sac and enter the brain during early embryogenesis. Upon entry, microglia undergo *in situ* proliferation and eventually colonize the entire brain by the third postnatal week in mice. However, the intricacies of their developmental expansion remain unclear. Here, we characterize the proliferative dynamics of microglia during embryonic and postnatal development using complementary fate-mapping techniques. We demonstrate that the developmental colonization of the brain is facilitated by clonal expansion of highly proliferative microglial progenitors that occupy spatial niches throughout the brain. Moreover, the spatial distribution of microglia switches from a clustered to a random pattern between embryonic and late postnatal development. Interestingly, the developmental increase in microglial numbers follows the proportional growth of the brain in an allometric manner until a mosaic distribution has been established. Overall, our findings offer insight into how the competition for space may drive microglial colonization by clonal expansion during development.

INTRODUCTION

Microglia, the brain's parenchymal macrophages, primarily derive from yolk sac macrophages which are generated at embryonic day 7.5 (E7.5) in mice and appear first within the brain at around E9.5.[1,2] The number of infiltrating yolk sac macrophages is dramatically reduced following the establishment of the blood-brain barrier at E14.5.[3,4] The entry of "foreign" microglial precursors is crucial for normal brain development processes: microglial cells participate in the wiring of neuronal networks through the pruning of dopaminergic axons and the establishment of the correct positioning of interneurons in their respective laminae[5]; they support myelination[6] and clear myelin debris and apoptotic cells[7]; and they promote the maturation and differentiation of neurons and oligodendrocytes.[8,9]

In mice, the majority of microglial cells are born during the first two postnatal weeks, reflected by a peak in their proliferation followed by a notable rise in cell numbers.[2,10–13] Following the developmental expansion phase, stable densities of microglia are eventually achieved in a region-specific manner through a fine-tuned balance of proliferation and apoptosis-driven refinement of microglial numbers.[12,14,15] There are two possibilities for how the population expands: the first comes from sequencing studies which show several clusters of microglia with a transcriptomic profile enriched in cell-cycle and proliferation-related genes, suggesting a unique proliferative capacity for these cells during development.[16–18] Another possibility is that all microglial precursors share the same propensity to proliferate, akin to the reported kinetics of microglia in the adult brain whereby microglia proliferate in a stochastic manner that is not restricted to a progenitor niche.[12,19] In contrast to this steady-state model of turnover, the microglial population is suggested to undergo context-dependent clonal expansion in response to both acute[19] and chronic insults,[20] resulting in a significant increase in the density of microglia.

Microglial proliferation during development can be driven by canonical mitogenic signaling via the CSF1/CSF1R axis.[5] Another potential driver of microglial proliferation is the availability of space whereby in the presence of unoccupied spatial niches, microglia will proliferate until a level of contact inhibition is achieved similar to what has been observed in depletion/repopulation paradigms,[21] although this mechanism of expansion has not been studied during development. Indeed, a hallmark of microglia in the adult brain is their "mosaic-like" distribution

throughout the parenchyma, which allows them to survey their local environment in a territorial fashion without input from neighboring cells.[22] However, how this mosaic distribution is achieved is yet to be uncovered and studied within the framework of microglial developmental dynamics.

In contrast to this regular adult mosaic distribution, the topographical distribution of microglia during development is heterogeneous, with accumulation of microglial cells in various neuronal progenitor niches throughout the brain including the deep layers of the cortex and various axonal tracts such as the corpus callosum.[5] These hotspots of microglia were traditionally referred to as ''fountains of microglia'' and were thought to represent regions of substantial infiltration of microglial precursors from the periphery.[23] It is now appreciated that the topographical placement of microglia during development is influenced by their local functions and interactions with the cellular milieu of the developing brain. A notable example is within the embryonic forebrain, where microglia transiently associate with axonal tracts of dopaminergic neurons and play a vital role in modulating proper wiring of neuronal networks at this early stage.[5] The extent to which these interactions dictate the final placement/colonization of the microglial population during development remains to be seen.

While there have been a number of exciting findings in regard to the developmental kinetics of the microglial population, it still remains unclear how their expansion is orchestrated in a relatively short period and how they achieve their final mosaic-like distribution. A pivotal question is whether a highly proliferative niche of microglia exists or whether each progenitor shares an equal propensity to proliferate. Here, we used a combined fate-mapping approach and applied a battery of spatial analyses to investigate whether microglia clonally expand during development and how the spatial distribution of microglia changes during development. Furthermore, we wanted to see how the concept of space availability impacts onto the expansion of microglia.

Our findings support the notion that the early expansion of the microglial population is coupled to the growth of the brain and space availability until a stable mosaic distribution is achieved. The developmental expansion of microglia is facilitated by clonal growth of embryonic progenitors, which colonize the entire parenchyma. Finally, using an RGB marking strategy, we uncover the clonal nature of the dynamics of microglia, revealing specific cells with high proliferative potential. Our data show that the relatively ''homogeneous'' mosaic of microglia in the adult brain is composed of a diverse array of interlocking clones which differ by size and regional association.

RESULTS

The developmental expansion of microglia follows an allometric growth coupled to the relative change in brain area

We set out to characterize the spatiotemporal changes in microglia that are associated with development of the population. We used the lineage-defining transcription factor PU.1 to map the changes in density and distribution of microglia across the embryonic forebrain, midbrain, and hindbrain. All PU.1$^+$ microglia (Figure 1A) were counted in these areas and, overall, we observed a remarkable stability in the density of microglia between E10.5 and E18.5 in the forebrain and midbrain (Figure 1B). We also found that the microglial expansion is coupled to the rate of growth in brain area (Figure 1B). This trend was not observed in the hindbrain, with the density of microglia significantly peaking during early embryonic (E10.5 and E12.5) and late embryonic (E18.5) development (Figure 1B). Moreover, analysis of the proliferative index of embryonic microglia (IBA1$^+$ Ki67$^+$/IBA1$^+$) indicated that microglial proliferation was largely stable between E10.5 and E16.5 (Figure 1C). In contrast to embryonic development, the density of PU.1$^+$ microglia rapidly increased in the postnatal forebrain, with postnatal day 14 (P14) brain presenting higher densities than P0 or P21 brains (Figure 1D). By P21, there was a non-significant drop in the density of microglia in line with a reported refinement of the population.[11,12,14] Interestingly, this trend was not observed when analyzing the average change in numbers, suggesting that the increase in forebrain size may contribute to an overall decrease in density by P21, similar to what was reported in the basal ganglia.[14] Again, it was observed that the microglial expansion is coupled to the rate of growth in brain area. Taken together, these findings suggest that microglial expansion follows an allometric growth curve that is coupled to the changes in brain growth.

The mosaic distribution is achieved by late postnatal development coinciding with the leveling of microglial density

Having observed that changes in microglial numbers closely follow the changes in brain size, we sought to investigate in detail the relationship between microglial density and the spatial distribution of these cells. Heterogeneous spatial trends were observed among embryonic microglia, characterized by either a clustered distribution or a dispersed distribution throughout the brain (Figure 1E). In contrast to the trends observed during embryonic and early postnatal development, microglia assumed an even spatial distribution by P21 (Figure 1F). This distribution was particularly notable in the cerebral cortex and is in line with the reported mosaic or tiled distribution of microglia in the adult brain. In-depth spatial analysis was carried out using Ripley's K function (K(r)). In brief, K(r) was calculated for the spatial points based on the xy coordinates of PU.1$^+$-labeled microglia (observed) and compared with a set of randomly generated spatial points (theoretical) for the same window, assuming a Poisson distribution. An observed K(r) value that is greater than the corresponding theoretical K(r) value indicates that those points are clustered. Conversely, a dispersed distribution is assumed when the observed K(r) is less than the corresponding theoretical K(r). Time-course analysis of the microglial K(r) revealed that the spatial dynamics of microglia vary during development, with several observed shifts between a clustered to a random distribution at E11.5–E12.5, E18.5–P0, and P14–P21 (Figure 1G). Several factors likely contribute to these changes in spatial dynamics, including the overall colonization behavior of microglia and their specific developmental functions and intercellular interactions, as microglia are highly receptive cells engaging in multiple forms of cell-to-cell communication.

The heterogeneous distribution of microglia during development is in stark contrast to their reportedly regular distribution

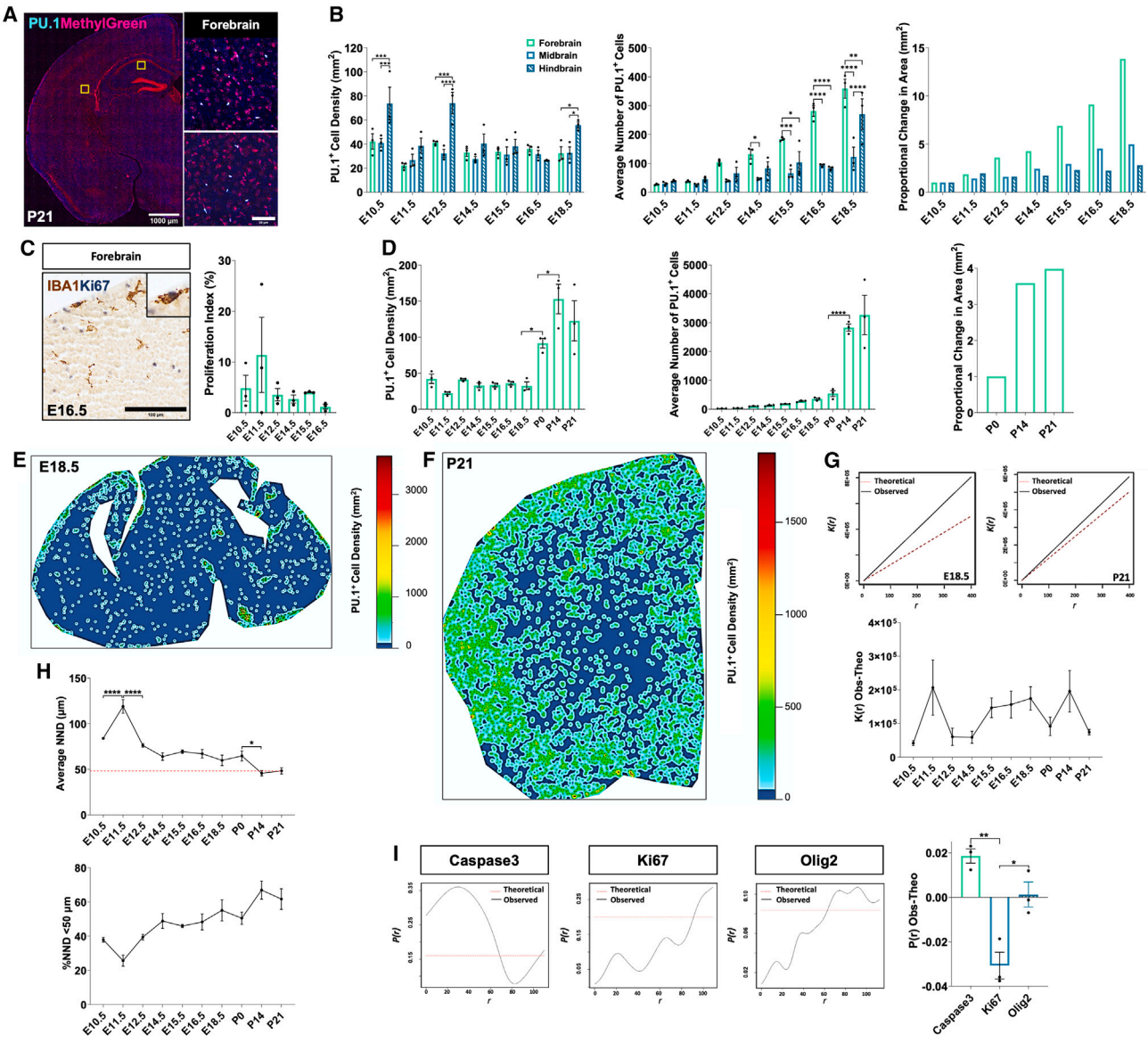

Figure 1. The spatiotemporal dynamics of microglia throughout development

(A) Representative image of PU.1$^+$ cells at P21 in the forebrain (images inverted).

(B) Time-course analysis of the number of PU.1$^+$ microglia in the forebrain, midbrain, and hindbrain, and proportional change in area during embryonic development.

(C) Representative images of IBA1$^+$ Ki67$^+$ cells in the forebrain, and quantification of microglial proliferation index based on the percentage of IBA1$^+$ Ki67$^+$ cells during embryonic development.

(D) Time-course analysis of the number of PU.1$^+$ microglia in the forebrain, and proportional change in area during embryonic and postnatal development.

(E) Representative heatmap displaying the spatial distribution of PU.1$^+$ cells at E18.5.

(F) Representative heatmap displaying the spatial distribution of PU.1$^+$ cells at P21.

(G) Representative K(r) functions of PU.1$^+$ microglial cells at E18.5 and P21 displaying the theoretical K(r) (red line) and observed K(r) (black line). Quantification of normalized K(r) (observed − theoretical) of PU.1$^+$ microglia during development.

(H) Quantification of the average NND and %NND <50 μm of PU.1$^+$ cells during development.

(I) Calculation of P(r) (observed − theoretical) between caspase3$^+$, Ki67$^+$, and Olig2$^+$ cells with microglial cells at E16.5.

Data are expressed as mean ± SEM, n = 3 per group (1 litter per time point); two-way ANOVA followed by Tukey's post hoc analysis (B) and one-way ANOVA followed by Bonferroni's post hoc analysis between groups (I) and for pairwise comparisons (C, D, G, and H). Statistical differences: *p < 0.05, **p < 0.01, ***p < 0.001, ****p < 0.0001. Scale bars, 1,000 μm and 50 μm (A), 100 μm (C).

in the adult brain, which has been likened to that of a mosaic pattern characterized by an average nearest neighbor distance (NND) of 50 μm between cells.[22] Therefore, we investigated how the NND of microglia changes during development. We found that the average NND between microglia was highest during early embryonic development at E11.5 (Figure 1H). Following E11.5, there was a steady decline in the NND as development progressed and the density of microglia increased (Figure 1H). Notably, the average NND of microglia was lowest at P14 when the percentage of microglia in close proximity to neighboring cells (NND <50 μm) was highest at 67%, coinciding with the observed peak in microglial density at P14 (Figure 1H). Moreover, changes in the NND of microglia significantly positively correlated with changes in microglial cell density (Figures S2A and S2B).

To test whether the heterogeneous spatial profile of developmental microglia is influenced by their functions and/or interactions with other cell types, the MarkConnect function was computed to investigate the spatial relationship between microglia (PU.1$^+$ or IBA1$^+$) and either dying cells (caspase3$^+$), proliferating cells (Ki67$^+$), or oligodendrocyte precursor cells (OPCs) (Olig2$^+$), as recent studies have suggested that microglia interact with the aforementioned elements during development.[7,8,24] In brief, the MarkConnect function was used to test spatial dependence or independence between both cell types at E16.5 within the forebrain. Overall, we observed that microglia displayed a dependent relationship with caspase3$^+$ cells, whereas the distribution of microglia was independent of Ki67$^+$ or Olig2$^+$ cells (Figures 1I and S1), which is in contrast to a recent study reporting that microglia were localized to regions with a high density of OPCs.[8] Therefore, the cellular interactions between microglia with dying and proliferating cells may contribute to their dispersion throughout the brain.

Altogether, these findings suggest that the spatial profile of microglia during early development is highly dynamic and heterogeneous in contrast to P21, when the cells display an even mosaic distribution that is achieved following postnatal refinement of the population.

Inhibition of postnatal microglial apoptosis alters the mosaic of microglia

We aimed to test the interdependence of microglia density and the formation of the mosaic by using *Vav-Bcl2* mice, which we previously showed to have increased microglial density due to the overexpression of antiapoptotic protein BCL2.[12] In adult *Vav-Bcl2* mice, the density of microglia is significantly higher and the NND of microglia is significantly lower than that of microglia from wild-type mice, indicating that the spatial dynamics of microglia become altered in the face of overcrowding (Figures 2A and 2B). On average, microglia covered a significantly smaller territory, thus accommodating an elevated cell density while still maintaining a minimal overlap between cells (Figures 2A and 2B). We performed spatial analysis using the inverse form of K(r), L(r), and observed that the changes in NND and territory do not happen at the expense of altering the distribution, as *Vav-Bcl2* mice maintained a random distribution similar to wild-type mice (Figure 2C). These findings suggest that the typical mosaic distribution and spatiotemporal profile of microglia is directly influenced by space availability within the brain.

Sparsely labeled microglia expand symmetrically as clonal clusters from early embryogenesis

Our previous data on cell clustering indicated that the dynamics of the microglial population in development could be driven by local clonal expansion events. Therefore, we devised a protocol to achieve very sparse fate mapping of the embryonic microglial pool with an EGFP label using the *Cx3cr1*^{CreER};*Rosa*^{mTmG} mouse model. We induced recombination with a low dose of tamoxifen (12.5 mg/kg) at E10.5 to achieve a sparse level of GFP expression in CX3CR1$^+$ cells in subsequent offspring, as indicated by the initial optimization (Figure S3). Subsequent analysis of sparsely labeled microglia within the brain primordium was carried out at E11.5, E16.5, and P30 (Figure 3A). Notably, GFP$^+$ cells expressed PU.1$^+$ at embryonic and adult stages, indicating the induction of Cre-dependent labeling in microglia and myeloid cells (Figure 3B). At E11.5, GFP$^+$ microglia were found scattered throughout the brain as isolated singlets (Figures 3C and 3E) and had an estimated recombination rate of 6% (Figure S3D), indicating successful sparse labeling. Indeed, spatial analysis at E11.5 showed that GFP$^+$ microglia were dispersed with a very high NND between cells (Figure 3E). Expansion of these sparsely labeled microglia was evident at E16.5 and P30, as indicated by a significant increase in the density of GFP$^+$ microglia in all brain regions (forebrain, midbrain, and hindbrain) (Figure 3C).

Interestingly, we observed that the expansion of the GFP$^+$ microglial population was associated with a change in their spatial distribution as GFP$^+$ microglia were found in tight clusters at E16.5, suggesting a clonal expansion of the originally labeled isolated progenitors (Figure 3E). This change in spatial distribution was reflected by changes in the average NND and K(r) of microglia which decreased and increased, respectively, indicating a clustered distribution (Figures 3E and 3F). Surprisingly, we observed very large "clouds" of GFP$^+$ microglia at P30 which spanned entire anatomical areas (Figure 3E). This was unexpected considering the low level of initial labeling at E11.5. Although this technique did not allow us to investigate this further due to the likely spatial overlap of large clones, we speculate that there is a substantial level of dispersion to facilitate the widespread distribution of cells observed at P30. Moreover, these data also suggest that early embryonic microglia progenitors are highly proliferative, generating large numbers of daughter cells that are capable of colonizing the entire brain, perhaps across anatomical compartments. In support of this, we observed that the proliferative index of GFP$^+$ microglia was relatively high throughout development (Figure 3D). Further spatial analysis at P30 revealed that GFP$^+$ microglia continue to display a clustered distribution, as indicated by a positive average K(r) value. However, we observed a non-significant decrease of the %NND <50 μm and corrected K(r) over the first quartile, which indicates that the GFP$^+$-labeled cells are not found as close together and shift toward a more random distribution compared with E16.5 (Figures 3E and 3F).

Clonal analysis of sparsely labeled microglia was carried out at E11.5 and E16.5 under the assumption that spatially related GFP$^+$ cells derived from the same progenitor. The average size

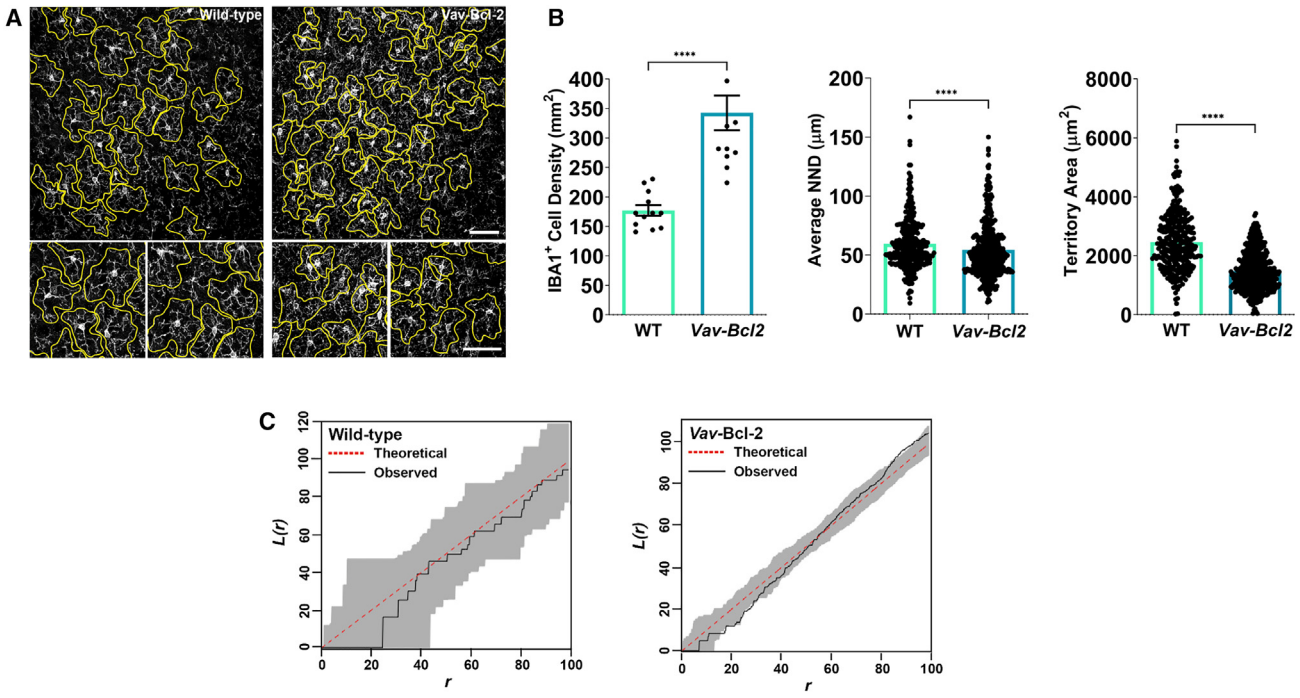

Figure 2. Impact of apoptosis deficiency on the establishment and maintenance of the microglial mosaic distribution

(A) Microglial territories were traced and measured in 30-µm z stacks of Iba1-labeled brain sections from adult (4–6 months) *Vav-Bcl2* mice (n = 4; 312 individual cells) and wild-type (n = 4; 470 individual cells) littermates. Scale bars, 100 µm.

(B) (Left) Quantification of microglial density (Iba1$^+$ cells) in the cortex of adult *Vav-Bcl2* mice and wild-type littermates. (Right) Quantification of microglial territory area (µm) in the cortex of *Vav-Bcl2* mice and wild-type littermates. (Center) Quantification of the regularity index of microglia in the cortex of *Vav-Bcl2* mice and wild-type littermates. NND, nearest neighbor distance.

(C) Representative plots of the L(r) derivative of Ripley's K statistics analyzing the spatial clustering of microglia from wild-type and *Vav-Bcl2* mice.

Data are presented as mean ± SEM. Data were analyzed with Student's t test. Statistical differences: ****p < 0.0005.

of GFP$^+$ clones increased significantly by E16.5, with a range of 1–7 cells per clone observed at E16.5 (Figure 3G). To gain insight into the fate of microglia, we applied the Markov model to the clonal data at E11.5 and E16.5 in order to test whether microglia are expanding symmetrically or asymmetrically, i.e., if newly born daughter cells continue to proliferate or whether they exit the cell cycle. Here, the clone-size distribution data at E16.5 fit a model whereby at least a portion of the population undergoes symmetric cell division (Figure 3H), which agrees with our findings that the microglial population expands exponentially during embryonic development.

Multicolor fate mapping reveals clonal expansion of postnatal microglia with a disparity in clone size

Our previous results suggested clonal expansion as a primary driver of the dynamics of the microglial population in development. To test this hypothesis more directly, we took advantage of RGB marking, a multicolor labeling strategy, which allows fate mapping of individual cells and their progeny. We first used SFFV-RGB vectors encoding the fluorescent proteins mCherry (red), Venus (green), and EBFP2 (blue) under the expression of the ubiquitous spleen form focus virus (SFFV) promoter. Because of the ubiquitous activity of the SFFV promoter, labeling is also expected in non-microglial populations.[25]

For postnatal fate mapping of the microglial population, the SFFV-RGB vectors were stereotactically injected into the lateral ventricle at P0 and analyzed at P21. Here, RGB-labeled microglia were evident in the parenchyma with labeled cells sharing the same RGB color hue, indicating clonal expansion of microglia from common parental cells (Figure 4A). The labeled microglia could be identified by their unique ramified morphology and co-expression of IBA1 (Figure S4A). Moreover, an exceptionally diverse color palette was observed (Figures 4A, 4B, S4B, and S4C), with an RGB color dispersion and distribution in line with *in vitro* transduction of N13 cells with SFFV-RGB vectors (Figure S5) and previous work in which RGB lentiviral vectors were used for clonal analysis.[26] To define clonal groups, we devised an *in vitro* assay using the N13 microglia cell line. In brief, SFFV-RGB-labeled N13 cells were seeded at very low densities (100–1,000 cells/well) to induce the growth of clonal colonies. The color spread (AU) in the RGB color space was calculated for each cluster. Overall, we observed that single-colored clusters had a low color spread (<11 AU), indicating that analysis of the RGB color space was sufficient for clonal discrimination (Figure S6). Therefore, we carried out a clonal analysis of labeled microglia at P21 whereby clones were defined as a group of microglial cells sharing the same color hue. Our analysis revealed that microglia give rise to clones of heterogeneous sizes, with the majority of clones consisting of between 1 and 5 cells

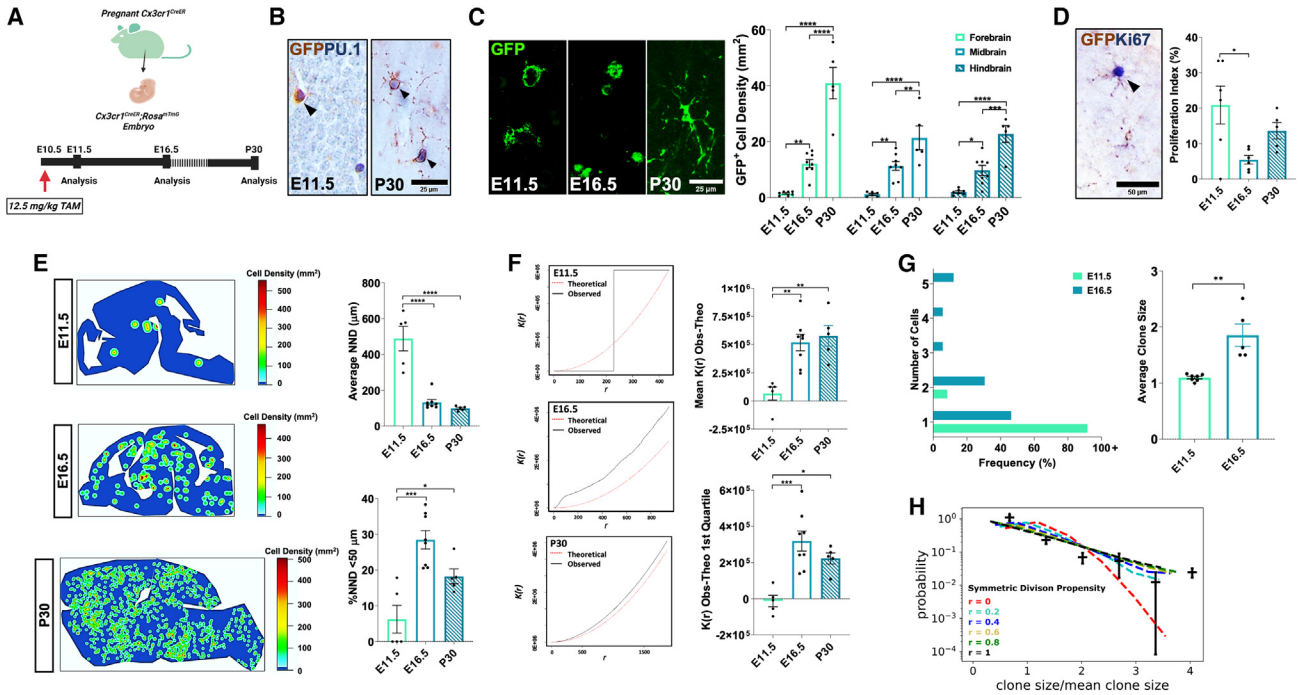

Figure 3. Sparse fate mapping of early embryonic microglia

(A) Experimental overview: induction of recombination in double transgenic Cx3cr1^{CreER};Rosa^{mTmG} embryos by pulsing Cx3cr1^{CreER} pregnant dams with 12.5 mg/kg TAM at E10.5 followed by analysis of resultant offspring at E11.5, E16.5, and P30.

(B) Representative images of brain parenchymal GFP$^+$ PU.1$^+$ cells at E11.5 and P30 in Cx3cr1^{CreER};Rosa^{mTmG} animals.

(C) Representative images of brain parenchymal GFP$^+$ cells (shown in green) at E11.5, E16.5, and P30 in Cx3cr1^{CreER};Rosa^{mTmG} animals. Time-course analysis of the density (cells/mm^2) of GFP$^+$ cells in the forebrain, midbrain, and hindbrain at E11.5 (n = 7), E16.5 (n = 8), and P30 (n = 5).

(D) Representative image of a GFP$^+$Ki67$^+$ cell at P30 and quantification of the proliferation index based on the percentage of GFP$^+$ Ki67$^+$ cells at E11.5 (n = 6), E16.5 (n = 6), and P30 (n = 5).

(E) Representative density maps of GFP$^+$ cells at E11.5, E16.5, and P30. Quantification of the average nearest neighbor distance (NND) and %NND <50 µm of GFP$^+$ cells at E11.5 (n = 5), E16.5 (n = 8), and P30 (n = 5).

(F) Representative K(r) functions of GFP$^+$ cells at E11.5 (n = 5), E16.5 (n = 8), and P30 (n = 5) displaying the theoretical K(r) (red line) and observed K(r) (black line). Quantification of normalized Ripley's K analysis (observed − theoretical) of GFP$^+$ cells over the entire K(r) function (upper panel) and over the first quartile (lower panel).

(G) Calculation of clone size frequency and average clone size at E11.5 (n = 7; 130 individual cells) and E16.5 (n = 5; 206 individual cells).

(H) Mathematical modeling based on clone-size frequency at E16.5 (black crosses representing standard deviation) against varying predictions of symmetric division propensity r (dashed lines; red: r = 0, cyan: r = 0.2, blue: r = 0.4, yellow: r = 0.6, green: r = 0.8, black: r = 1.0).

Data are expressed as mean ± SEM; two-way ANOVA followed by Tukey's post hoc analysis (C) or one-way ANOVA followed by Bonferroni's post hoc analysis (D, E, F), or Student's t test for independent means (G). Statistical differences: *p < 0.05, **p < 0.01, ***p < 0.001, ****p < 0.0001. Scale bars, 25 µm (B and C) and 50 µm (D).

(Figure 4C). In contrast, a smaller proportion of the clones consisted of much larger numbers of microglia of up to 28 cells, suggesting that there is a disparity in the proliferative index of labeled microglial cells, with some postnatal microglia expanding at a much greater rate than others and a portion of the population not engaging in proliferation in the postnatal brain (Figure 4C).

To validate and refine our approach, we next used mir-RGB vectors expressing either mCherry (red), Venus (green), or mTurquoise (blue) under the phosphoglycerate kinase (PGK) promoter, showing superior microglial specificity (in the adult brain 78.36% ± 12.06% of n = 185 RGB-positive cells in four mice were P2Y12-positive microglia: data not shown). The vectors were stereotactically injected into the lateral ventricle at P0 and analyzed at P30. RGB-labeled microglia were detected in the brain (Figure S4D) and, similarly to P21, clonal expansion of the RGB-labeled microglia could be seen (Figure 5A). We noted that the mir-RGB-labeled microglia at P30 were reminiscent of SFFV-RGB-labeled microglia, including the diverse array of RGB combinations among labeled microglia (Figures 5A, 5B, S4E, and S4F). Another feature of mir-RGB clones that mirrored SFFV-RGB clones was the heterogeneity in clone size, with the majority of clones consisting of <5 cells and a minority containing ≥15 cells, echoing the earlier finding that the proliferation rate of clones is not equal (Figure 5C). Altogether we found no significant differences between the average clone size at P21 (7 cells) and P30 (5 cells) (Figure 6A), indicating that the clonal dynamics of microglia remain stable during this window, which is in line with the reported stabilization of microglial numbers by the third postnatal week.[11,12]

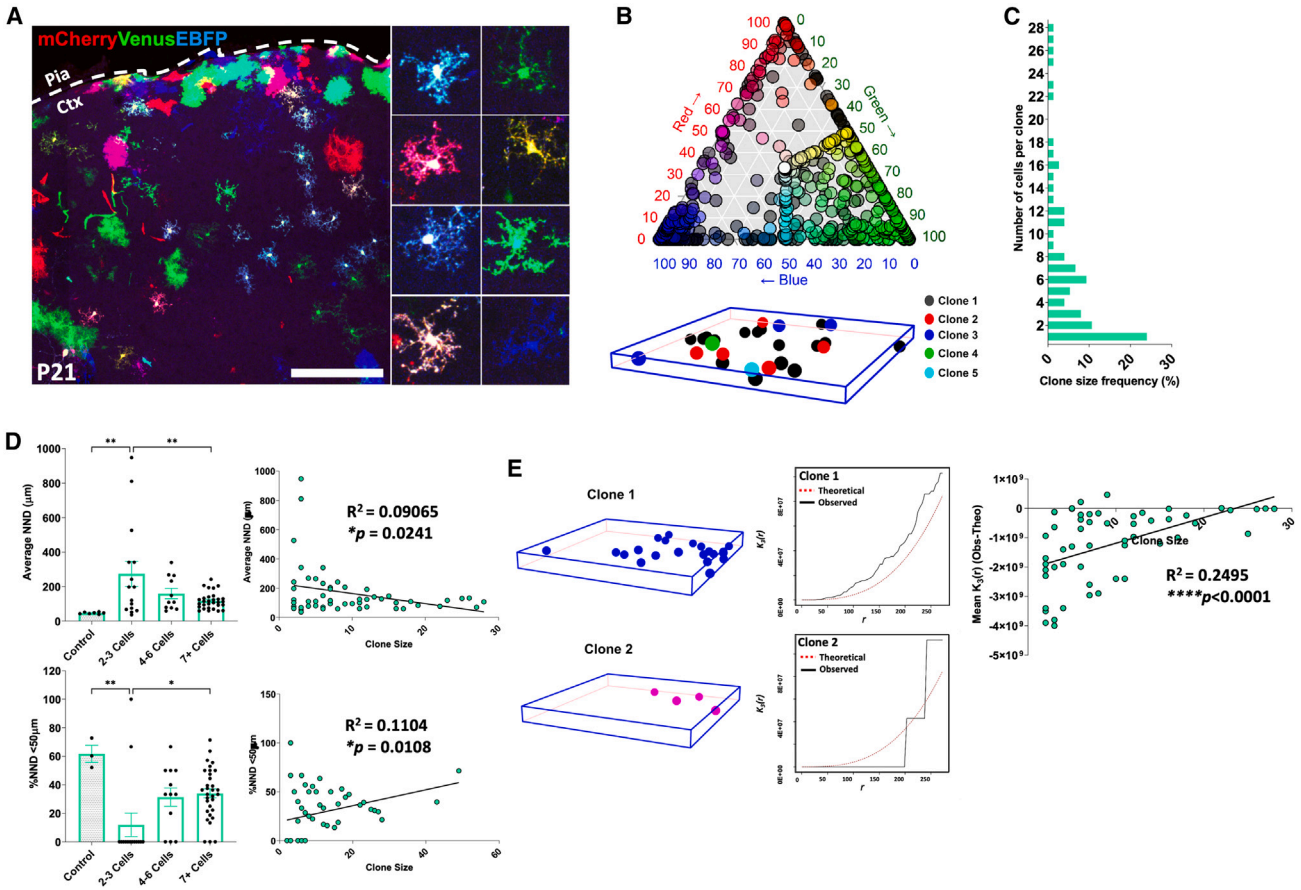

Figure 4. Multicolor marking of postnatal microglia up to P21 using SFFV-RGB vectors

(A) Representative images of SFFV-RGB-labeled cells in the cortex at P21 including ramified microglia. Scale bar, 200 μm.

(B) Ternary color space of SFFV-RGB-labeled microglia (n = 3; 618 individual cells) and representative 3D point pattern displaying the spatial distribution of SFFV-RGB-labeled microglia belonging to different clones.

(C) Quantification of clone-size frequency (%) at P21.

(D) Comparison of intraclonal NND (μm) and %NND <50 μm at P21 (n = 3, 56 clones) with total microglia population from adult mice (control; n = 7). Linear regression analysis of intraclonal NND (μm) and %NND <50 μm versus clone size at P21.

(E) Representative examples of a 3D point pattern for a large microglial clone (blue) and a smaller microglial clone (pink) with corresponding 3D K(r) function displaying the theoretical $K_3(r)$ (red line) and observed $K_3(r)$ (black line). Quantification of normalized K(r) (observed − theoretical) versus clone size at P21.

Data are expressed as mean ± SEM; one-way ANOVA followed by Bonferroni's post hoc analysis (D) or linear regression analysis and Pearson's correlation test (D and E). Statistical differences: *p < 0.05, **p < 0.01, ****p < 0.0001.

The microglial mosaic is made up of a diverse patchwork of microglial clones of varying proliferative potential

Next, we took advantage of our RGB marking approach to look more closely at a clonal level and thoroughly investigate the intricate cell-to-cell makeup of the microglial mosaic. At both P21 and P30 we observed a diverse array of spatial patterns among clones, with some appearing to be spatially organized according to clonal groups and others displaying "clonal mixing" with cells of different clones interlocking with others (Figures 4B and 5B). To objectively characterize the spatial organization of microglial clones, we calculated the average NND between cells of individual clones and compared it with the average NND of adult microglia (control). Interestingly, we found that the average NND of clonal microglia at both P21 (130 μm) and P30 (134 μm) is higher than that of control microglia (46 μm) (Figures 4D and 5D). Moreover, we observed no significant differences between the average NND distance of clonal microglia at P21 or P30, suggesting that the spatial distribution of clones is stable during the juvenile phase (Figure 6B). A similar trend was seen when we assessed the percentage of microglia with an NND of less than 50 μm in both clonal microglia and naive microglia, with 61% of naive microglia displaying an NND of <50 μm compared with 28% (P21) and 24% (P30) in clonal microglia (Figures 4D, 5D, and 6B).

Spatial analysis revealed a significant negative correlation clone size and the average NND of clones at both P21 and P30, indicating that microglial cells from larger clones typically have a smaller NND in comparison with those of smaller-sized clones which are further apart (Figures 4D and 5D). Similarly, we found a positive trend between clone size

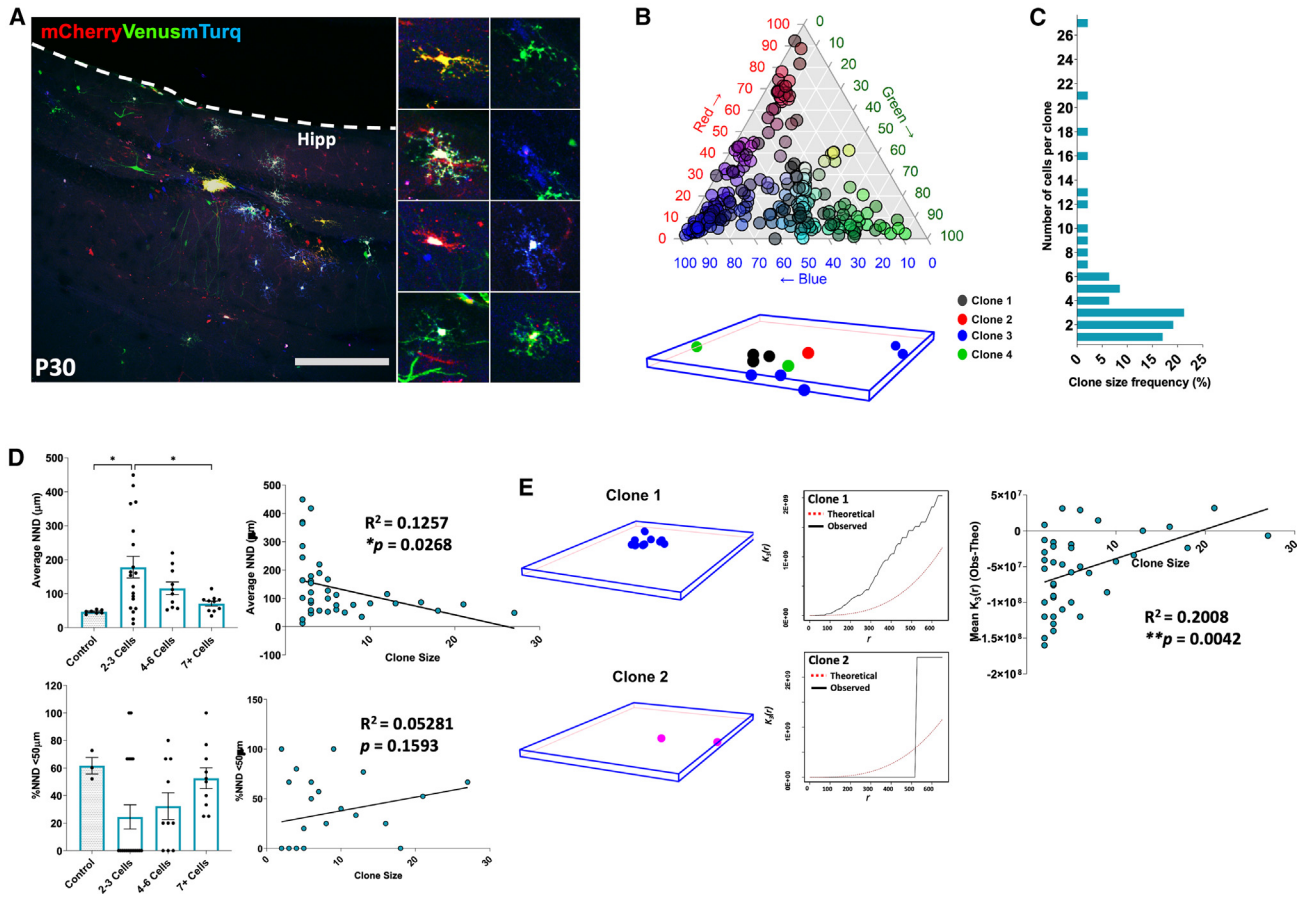

Figure 5. Multicolor marking of postnatal microglia until P30 using mir-RGB vectors

(A) Representative images of mir-RGB-labeled cells in the hippocampus at P30 including ramified microglia. Scale bar, 200 μm.

(B) Ternary color space of mir-RGB-labeled microglia (n = 5; 248 individual cells) and representative 3D point pattern displaying the spatial distribution of mir-RGB-labeled microglia belonging to different clones.

(C) Quantification of clone-size frequency (%) at P30.

(D) Comparison of intraclonal NND (μm) and %NND <50 μm at P30 (n = 5, 39 clones) with total microglia population from adult mice (control; n = 7). Linear regression analysis of intraclonal NND (μm) and %NND <50 μm versus clone size at P30.

(E) Representative examples of a 3D point pattern for a large microglial clone (blue) and a smaller microglial clone (pink) with corresponding 3D K(r) function displaying the theoretical $K_3(r)$ (red line) and observed $K_3(r)$ (black line). Quantification of normalized K(r) (observed − theoretical) versus clone size at P30.

Data are expressed as mean ± SEM; one-way ANOVA followed by Bonferroni's post hoc analysis (D) or linear regression analysis and Pearson's correlation test (D and E). Statistical differences: *p < 0.05, **p < 0.01.

and %NND < 50 μm, which reached statistical significance at P21 (Figures 4D and 5D). This finding indicates that microglia from larger clones display a spatial association, which we were able to confirm by applying the spatial statistics test, the K(r) function, to analyze our 3D stacks (Figures 4E and 5E). Here we found that larger clones were more clustered than smaller clones which were typically dispersed, as evidenced by a positive trend between clone size and the mean K(r) and normalized K(r), which reached significance at P21 (Figures 4E and 5E). In sum, we did not find any evidence of ordered organization of microglial clones. However, our spatial analyses suggest that larger clones dominate spatial niches within the microglial mosaic in comparison with smaller clones, which are dispersed and "diluted" throughout the network.

To gain insight into the proliferative kinetics of clonal microglia, we applied mathematical models to the clonal data at P21 and P30. We initially modeled the timing of cell-division initiation in microglia considering three models: (1) all microglia are actively dividing at the same time and clones are equipotent where no clone has a proliferative advantage (while individual cells may divide faster, any proliferative advantage is not inherited); (2) microglia are initially non-dividing and start dividing at random times, and clones are equipotent; and (3) microglia start dividing at the same time but with different proliferative activity, which is inherited along with a clone, i.e., some clones have a sustained proliferative advantage over others. For our modeling, we assumed that cell-division rates are uniformly distributed. We observed that model 1 did not fit the clonal data but both model 2 and model 3 did (Figure 6C).

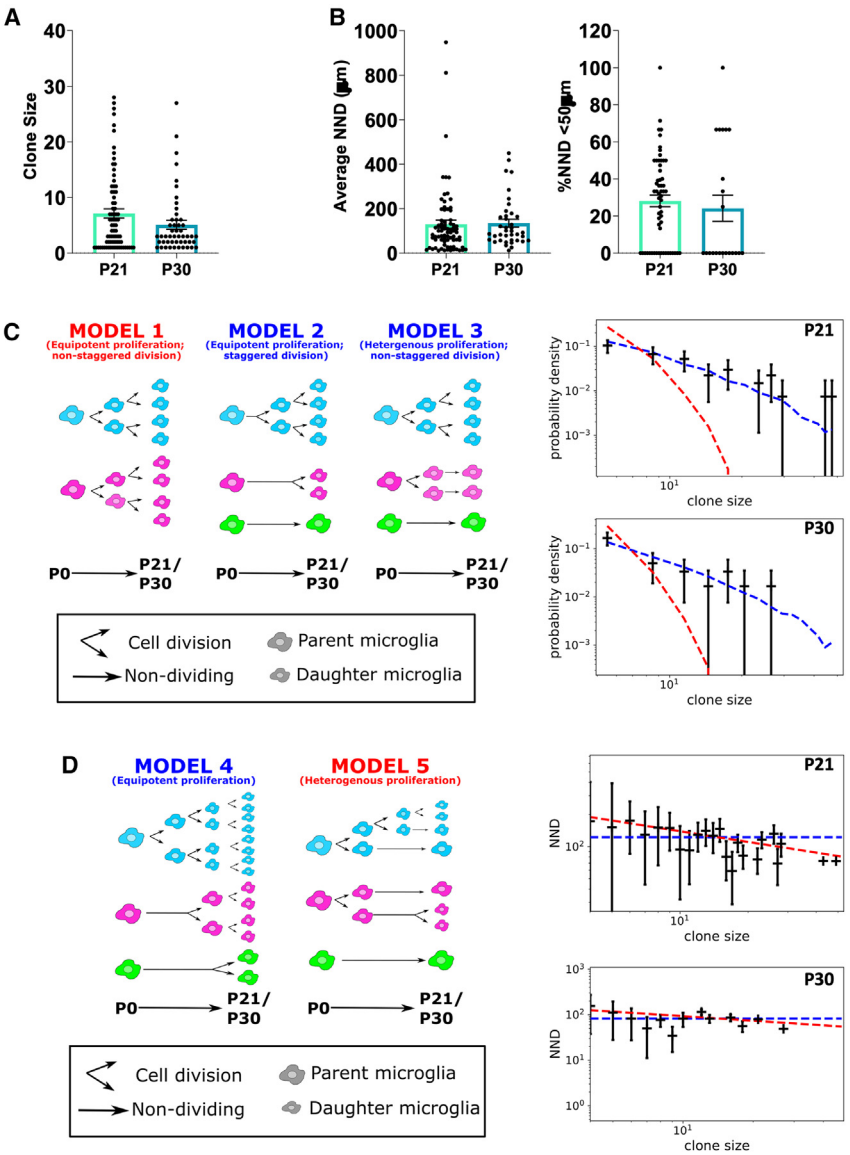

Figure 6. Mathematical modeling of microglial clonal dynamics at P21 and P30

(A) Comparison of the average microglial clone size between P21 (n = 3, 76 clones) and P30 (n = 5, 49 clones).

(B) Comparison of the average NND (μm) and %NND <50 μm between P21 (n = 3, 76 clones) and P30 (n = 5, 49 clones).

(C) Modeling the dynamics of cell-division initiation in microglia at P21 and P30 based on their clone-size distribution (black crosses representing standard deviation) against model 1 (red) and models 2 and 3 (blue).

(D) Modeling of proliferative dynamics of clonal microglia at P21 and P30 based on their NND (black crosses representing standard deviation) against predictions of model 4 (blue) and model 5 (red).

Data are expressed as mean ± SEM; Student's t test for independent means.

DISCUSSION

Understanding the proliferative mechanisms employed by the microglial population in both development and disease has garnered considerable interest in recent years.[19,27–29] In the healthy brain, resident microglia self-renew in a stochastic manner throughout life, with varying rates of turnover in different brain regions.[12,19,28,30] In response to any deviation from homeostasis such as in disease[19,20] and in depopulation-repopulation paradigms,[21,31] microglia increase their rate of proliferation and may undergo clonal expansion in order to increase their cell numbers. Here, we expand our understanding of the proliferative dynamics of microglia during development and demonstrate for the first time that developmental growth of the microglial population is facilitated by clonal expansion of early precursors during embryonic and postnatal developments, which form an intricate patchwork of clones within the microglial mosaic. Moreover, the general expansion of microglia can be described as allometric, whereby the increase in microglial numbers is proportional to the increasing size of the brain.

Hence, we excluded model 1 whereby equipotent cell division was initiated in all microglia at the same time. To distinguish between models 2 and 3, we utilized an additional analytical model based on the NND data of cells within clones. For this approach, we considered two more models: (4) microglia are equipotent and may initiate proliferation at any time (no distinction between model variants 1 and 2 above); and (5) the proliferative potential of individual microglia is heterogeneous. Here, we found that the models did not significantly vary from the data; however, model 2 produced a better fit for the data, suggesting that the proliferative potential is heterogeneous among microglial clones (Figure 6D). In sum, our data suggest that the proliferative potential of microglia in the developing brain is heterogeneous and that daughter cells arising from highly proliferating progenitors spatially associate within the mosaic network in a territorial fashion.

The number of studies investigating clonal dynamics in microglia is limited, mainly due to technological limitations associated with multicolor reporter lines, seen for example in the Confetti strain.[19,21] While such studies have been informative, the Confetti model, for example, is limited to four color combinations and therefore lacks the resolution to provide an in-depth clonal analysis. Here we used a combination of SFFV- and mir-RGB vectors to label microglia in the postnatal brain, which resulted in a multitude of color combinations and thus allowed us to thoroughly characterize the clonal dynamics of these cells. Our subsequent clonal analysis unveiled heterogeneity in clone size, with

a small subset of microglia generating very large clones. This suggests a considerable degree of clonal variability linked to proliferative potential: final clonal size will be instructed by the proliferation capacity of the originally labeled parent cells and then their progeny. Interestingly, similar proliferative heterogeneity has also been reported in a model of microglial depletion/repopulation in the visual cortex.[32] In the context of the existing literature our findings raise a number of questions, including the source of this proliferative diversity and whether or not this is a long-term feature of individual microglial cells that is carried through until adulthood.

We also utilized a method of sparse labeling to track the progeny of individual microglia from early embryogenesis. Our findings indicate that some individual microglia undergo substantial expansion, as evidenced by the clouds of sparse-labeled microglia at P30. This finding is in line with a recent study in which *in vivo* barcoding was used to track clonal expansion of various cell types, including microglia, within the embryonic brain.[33] In line with our findings, this study showed that expanded microglial progenitors span anatomical niches almost in a continuum.[33] Here we examined the changes in the spatial distribution of sparsely labeled microglia, which were highly clustered during embryonic development in comparison with adulthood, when the labeled microglia were more randomly distributed with a lower NND in line with the formation of the mosaic, similar to the trends observed in the total PU.1$^+$ population. The drivers of these changes in spatial distribution remain unclear, although our data and those of others suggest that the attraction and repulsion of microglia to either dying or proliferating cells may facilitate microglial dispersion during development.[7,24,34] In this regard, we observed that RGB-marked clones displayed a level of spatial mixing, indicating that the microglial mosaic is not made up of strict clonal units. However, spatial analysis of RGB clones revealed that larger clones tended to be closer together in space, thus begging the question of whether there is a level of clonal dominance in certain niches throughout the brain. This may be important if functional mutations were inherited by daughter cells of specific clones, which may render certain spatial niches vulnerable to microglial functional diversity.

An interesting observation from this study was the apparent relationship between microglial expansion and space availability. Our results suggest that there is a coupling between the rate of microglial expansion and the growth rate of the brain, resulting in a plateaued cellular density during embryonic development. A similar plateau was reported in a recent study where the changes in microglial density were investigated in the hypothalamus.[8] The mathematical modeling applied here supports the notion that during embryonic development there is an exponential growth phase during which microglia primarily undergo symmetric divisions similar to what has been observed during embryogenesis in the zebrafish.[35] In contrast to embryonic development, we observed a remarkable increase in the number and density of microglia during postnatal life with a peak in microglial density at P14, in line with previous reports.[2,6,11] Interestingly, the increase in cell number still tracks a trend of increasing brain area. This type of growth in a cell population is referred to as allometric growth, which is reported in a variety of cell types across species and is important for regulating the size of certain organs.[36] The phenomenon of allometric growth is not thoroughly understood and is thought to be influenced by both intrinsic and extracellular mechanisms of growth control.[36] The intricate connection of niche availability and stemness potential has recently been defined as a mechanism of ''crowding feedback,'' whereby under suitable feedback regulation the property of ''stemness'' is entirely determined by the cell environment.[37]

Indeed, in further support of this hypothesis, we found that changes in the density of microglia correlated with changes in the NND of cells. This suggests that the density of microglia will increase during development until cells become associated with each other, in other words when there is equilibrium, and the mosaic network is achieved. This observation sheds light on the reported ability of microglia to recapitulate their normal densities and spatiotemporal distribution following depletion in several paradigms.[21,31,38] Considering the interplay between brain growth and microglial expansion, it is not unreasonable to predict that space availability may favor the expansion of certain microglial progenitors over others that are spatially constricted, and thus may explain the observed disparity in clone size at P21 and P30.

Furthermore, these findings suggest contact inhibition as an underlying mechanism. Contact inhibition is a process of allometric growth control that has been described in cell culture and cancer cells, whereby cells will expand and migrate freely until they come into contact with another cell or physical barrier.[39–41] The mechanisms of contact inhibition are thought to rely on membrane-bound cell adhesion molecules (CAMs) such as E-cadherin. For example, loss of E-cadherin disrupts contact inhibition, resulting in metastasis of epidermal cells.[42] Currently there are limited data regarding potential pathways regulating contact inhibition in microglia, and it is unclear whether CAMs are involved in this. One potential transmembrane proteoglycan which may be involved is syndecan-4, which has been previously implicated in regulating contact inhibition in mesenchymal cells.[43] Interestingly, it was observed that syndecan-4 is downregulated in microglia following their depletion, which led the authors to suggest a potential role for syndecan-4 in regulating microglial contact inhibition.[21] Other potential sources of allometric growth control are spatial checkpoints in the cell cycle such as those reported between the G_1 and S phase in epithelial cells, which will prevent proliferation when cells become spatially restricted.[44]

Taken together, our findings demonstrate that the developmental expansion of microglia is driven by clonal expansion of early invading microglial progenitors, with a small proportion generating relatively large clones. The density of microglia rapidly increases during postnatal development until a relatively even spatial distribution and the microglial mosaic are achieved. In addition, spatial analysis reveals that the microglial mosaic is fashioned from an intricate patchwork of diverse microglial clones. These findings uncover another layer of the proliferative capabilities of microglia and thus will be useful for understanding the behavior of these cells during neurodevelopmental and neurological diseases.

Limitations of the study

While performing fate mapping of microglia using sparse labeling, our data would point to potentially different recombination

efficiency in proliferative versus non-proliferative embryonic microglia. Our analyses could not unpick this directly, but the observed population dynamics over time would be supportive of the hypothesis that cells with enhanced stemness were preferentially recombined. Over time these would take over the population, becoming over-represented when compared with their contribution at earlier points in development. Our data could not provide definitive support for this idea, nor could the mathematical modeling of the data.

Another limitation worth highlighting is the fact that the mathematical modeling of clonal populations in the postnatal brain could not ascertain whether the differential expansion potential was an intrinsic property of cells or, rather, a property regulated by the local microenvironment. While it is likely that a combination of these factors is the underlying source of proliferative potential, our present data did not provide empirical evidence to support either of these options.

STAR★METHODS

Detailed methods are provided in the online version of this paper and include the following:

- KEY RESOURCES TABLE
- RESOURCE AVAILABILITY
  - Lead contact
  - Materials availability
  - Data and code availability
- EXPERIMENTAL MODEL AND SUBJECT DETAILS
  - Animals
  - Cell lines
- METHOD DETAILS
  - Induction of cre-dependent sparse labelling of microglia with EGFP
  - Multicolour fate mapping with RGB vectors
  - Immunohistochemistry
  - Image acquisition and analysis
  - Analysis of microglia transduced with RGB vectors
  - Spatial analysis using SpatStat
  - Nearest neighbor analysis
  - 2-D Ripley's K spatial analysis
  - 3-D Ripley's K spatial analysis
  - Marked connect function of multitype point patterns
- QUANTIFICATION AND STATISTICAL ANALYSIS

SUPPLEMENTAL INFORMATION

Supplemental information can be found online at https://doi.org/10.1016/j.celrep.2023.112425.

ACKNOWLEDGMENTS

We thank the Southampton Flow Cytometry Facility and the Imaging Unit for technical advice and the Biomedical Research Facility for assistance with animal breeding and maintenance. We thank Georgina Dawes for technical assistance and Maria Olmedillas del Moral, Cris Richter, and Bianca Brawek for analyses of the specificity of mir-RGB vectors. We thank Professor Mark Cragg for provision of *Vav-Bcl2* mice, and Dr. Salah Elias for provision of *Rosa*$^{mT/mG}$ mice. The research was funded by the Leverhulme Trust (RPG-2016-311), the Medical Research Council (MR/P024572/1), and the Deutsche Forschungsgemeinschaft (SFB841/SP01 to K.R. and B.F.).

AUTHOR CONTRIBUTIONS

D.G.-N. designed the study, secured the funding, and supervised the project. L.B.-C. performed most of experiments and analyzed the data. A.R.M. and K.E.A. contributed experimental work and analysis. K.R. and B.F. provided SFFV-RGB vectors. K.L. and O.G. provided the mir-RGB vectors. P.G. performed mathematical modeling of the data. L.B.-C., D.A.M., and D.G.-N. wrote the manuscript. All authors contributed to drafting and read and approved the final manuscript.

DECLARATION OF INTERESTS

The authors declare no competing interests.

INCLUSION AND DIVERSITY

We support inclusive, diverse, and equitable conduct of research.

Received: July 27, 2022
Revised: January 25, 2023
Accepted: April 6, 2023

REFERENCES

1. Ginhoux, F., Greter, M., Leboeuf, M., Nandi, S., See, P., Gokhan, S., Mehler, M.F., Conway, S.J., Ng, L.G., Stanley, E.R., et al. (2010). Fate mapping analysis reveals that adult microglia derive from primitive macrophages. Science *330*, 841–845. https://doi.org/10.1126/science.1194637.
2. Alliot, F., Godin, I., and Pessac, B. (1999). Microglia derive from progenitors, originating from the yolk sac, and which proliferate in the brain. Brain Res. Dev. Brain Res. *117*, 145–152. https://doi.org/10.1016/S0165-3806(99)00113-3.
3. Stremmel, C., Schuchert, R., Wagner, F., Thaler, R., Weinberger, T., Pick, R., Mass, E., Ishikawa-Ankerhold, H.C., Margraf, A., Hutter, S., et al. (2018). Yolk sac macrophage progenitors traffic to the embryo during defined stages of development. Nat. Commun. *9*, 75. https://doi.org/10.1038/s41467-017-02492-2.
4. Ranawat, N., and Masai, I. (2021). Mechanisms underlying microglial colonization of developing neural retina in zebrafish. Elife *10*, e70550. https://doi.org/10.7554/eLife.70550.
5. Squarzoni, P., Oller, G., Hoeffel, G., Pont-Lezica, L., Rostaing, P., Low, D., Bessis, A., Ginhoux, F., and Garel, S. (2014). Microglia modulate wiring of the embryonic forebrain. Cell Rep. *8*, 1271–1279. https://doi.org/10.1016/j.celrep.2014.07.042.
6. Wlodarczyk, A., Holtman, I.R., Krueger, M., Yogev, N., Bruttger, J., Khorooshi, R., Benmamar-Badel, A., de Boer-Bergsma, J.J., Martin, N.A., Karram, K., et al. (2017). A novel microglial subset plays a key role in myelinogenesis in developing brain. EMBO J. *36*, 3292–3308. https://doi.org/10.15252/embj.201696056.
7. Cunningham, C.L., Martínez-Cerdeño, V., and Noctor, S.C. (2013). Microglia regulate the number of neural precursor cells in the developing cerebral cortex. J. Neurosci. *33*, 4216–4233. https://doi.org/10.1523/JNEUROSCI.3441-12.2013.
8. Marsters, C.M., Nesan, D., Far, R., Klenin, N., Pittman, Q.J., and Kurrasch, D.M. (2020). Embryonic microglia influence developing hypothalamic glial populations. J. Neuroinflammation *17*, 146. https://doi.org/10.1186/s12974-020-01811-7.
9. Decoeur, F., Picard, K., St-Pierre, M.-K., Greenhalgh, A.D., Delpech, J.-C., Sere, A., Layé, S., Tremblay, M.-E., and Nadjar, A. (2022). N-3 PUFA deficiency affects the ultrastructural organization and density of white matter

microglia in the developing brain of male mice. Front. Cell. Neurosci. *16*, 802411. https://doi.org/10.3389/fncel.2022.802411.

10. Askew, K., and Gomez-Nicola, D. (2018). A story of birth and death: insights into the formation and dynamics of the microglial population. Brain Behav. Immun. *69*, 9–17. https://doi.org/10.1016/j.bbi.2017.03.009.
11. Nikodemova, M., Kimyon, R.S., De, I., Small, A.L., Collier, L.S., and Watters, J.J. (2015). Microglial numbers attain adult levels after undergoing a rapid decrease in cell number in the third postnatal week. J. Neuroimmunol. *278*, 280–288. https://doi.org/10.1016/j.jneuroim.2014.11.018.
12. Askew, K., Li, K., Olmos-Alonso, A., Garcia-Moreno, F., Liang, Y., Richardson, P., Tipton, T., Chapman, M.A., Riecken, K., Beccari, S., et al. (2017). Coupled proliferation and apoptosis maintain the rapid turnover of microglia in the adult brain. Cell Rep. *18*, 391–405. https://doi.org/10.1016/j.celrep.2016.12.041.
13. De, S., Van Deren, D., Peden, E., Hockin, M., Boulet, A., Titen, S., and Capecchi, M.R. (2018). Two distinct ontogenies confer heterogeneity to mouse brain microglia. Development *145*, dev152306. https://doi.org/10.1242/dev.152306.
14. Hope, K.T., Hawes, I.A., Moca, E.N., Bonci, A., and De Biase, L.M. (2020). Maturation of the microglial population varies across mesolimbic nuclei. Eur. J. Neurosci. *52*, 3689–3709. https://doi.org/10.1111/ejn.14740.
15. Menassa, D.A., Muntslag, T.A.O., Martin-Estebané, M., Barry-Carroll, L., Chapman, M.A., Adorjan, I., Tyler, T., Turnbull, B., Rose-Zerilli, M.J.J., Nicoll, J.A.R., et al. (2022). The spatiotemporal dynamics of microglia across the human lifespan. Dev. Cell *57*, 2127–2139.e6. https://doi.org/10.1016/j.devcel.2022.07.015.
16. Hammond, T.R., Dufort, C., Dissing-Olesen, L., Giera, S., Young, A., Wysoker, A., Walker, A.J., Gergits, F., Segel, M., Nemesh, J., et al. (2019). Single-cell RNA sequencing of microglia throughout the mouse lifespan and in the injured brain reveals complex cell-state changes. Immunity *50*, 253–271.e6. https://doi.org/10.1016/j.immuni.2018.11.004.
17. Li, Q., Cheng, Z., Zhou, L., Darmanis, S., Neff, N.F., Okamoto, J., Gulati, G., Bennett, M.L., Sun, L.O., Clarke, L.E., et al. (2019). Developmental heterogeneity of microglia and brain myeloid cells revealed by deep single-cell RNA sequencing. Neuron *101*, 207–223.e10. https://doi.org/10.1016/j.neuron.2018.12.006.
18. Masuda, T., Sankowski, R., Staszewski, O., Böttcher, C., Amann, L., Scheiwe, C., Nessler, S., Kunz, P., van Loo, G., et al. (2019). Spatial and temporal heterogeneity of mouse and human microglia at single-cell resolution. Nature *566*, 388–392. https://doi.org/10.1038/s41586-019-0924-x.
19. Tay, T.L., Mai, D., Dautzenberg, J., Fernández-Klett, F., Lin, G., Datta, M., Drougard, A., Stempfl, T., Ardura-Fabregat, A., et al. (2017). A new fate mapping system reveals context-dependent random or clonal expansion of microglia. Nat. Neurosci. *20*, 793–803. https://doi.org/10.1038/nn.4547.
20. Jordão, M.J.C., Sankowski, R., Brendecke, S.M., Locatelli, G., Tai, Y.H., Tay, T.L., Schramm, E., Armbruster, S., Hagemeyer, N., et al. (2019). Single-cell profiling identifies myeloid cell subsets with distinct fates during neuroinflammation. Science *363*, eaat7554. https://doi.org/10.1126/science.aat7554.
21. Zhan, L., Krabbe, G., Du, F., Jones, I., Reichert, M.C., Telpoukhovskaia, M., Kodama, L., Wang, C., Cho, S.-h., Sayed, F., et al. (2019). Proximal recolonization by self-renewing microglia re-establishes microglial homeostasis in the adult mouse brain. PLoS Biol. *17*, e3000134. https://doi.org/10.1371/journal.pbio.3000134.
22. Nimmerjahn, A., Kirchhoff, F., and Helmchen, F. (2005). Resting microglial cells are highly dynamic surveillants of brain parenchyma in vivo. Science *308*, 1314–1318. https://doi.org/10.1126/science.1110647.
23. Río-Hortega. (1919). El "tercer elemento" de los centros nerviosos. I. La microglía en estado normal. II. Intervención de la microglía en los procesos patológicos (células en bastoncito y cuerpos gránulo-adiposos). Bol. Soc. Esp. Biol . *VIII*, 69–109.
24. Hattori, Y., Naito, Y., Tsugawa, Y., Nonaka, S., Wake, H., Nagasawa, T., Kawaguchi, A., and Miyata, T. (2020). Transient microglial absence assists postmigratory cortical neurons in proper differentiation. Nat. Commun. *11*, 1631. https://doi.org/10.1038/s41467-020-15409-3.
25. Gomez-Nicola, D., Riecken, K., Fehse, B., and Perry, V.H. (2014). In-vivo RGB marking and multicolour single-cell tracking in the adult brain. Sci. Rep. *4*, 7520. https://doi.org/10.1038/srep07520.
26. Weber, K., Thomaschewski, M., Warlich, M., Volz, T., Cornils, K., Niebuhr, B., Täger, M., Lütgehetmann, M., Pollok, J.-M., Stocking, C., et al. (2011). RGB marking facilitates multicolor clonal cell tracking. Nat. Med. *17*, 504–509. https://doi.org/10.1038/nm.2338.
27. Gómez-Nicola, D., Fransen, N.L., Suzzi, S., and Perry, V.H. (2013). Regulation of microglial proliferation during chronic neurodegeneration. J. Neurosci. *33*, 2481–2493. https://doi.org/10.1523/JNEUROSCI.4440-12.2013.
28. Füger, P., Hefendehl, J.K., Veeraraghavalu, K., Wendeln, A.-C., Schlosser, C., Obermüller, U., Wegenast-Braun, B.M., Neher, J.J., Martus, P., Kohsaka, S., et al. (2017). Microglia turnover with aging and in an Alzheimer's model via long-term in vivo single-cell imaging. Nat. Neurosci. *20*, 1371–1376. https://doi.org/10.1038/nn.4631.
29. Hammond, B.P., Manek, R., Kerr, B.J., Macauley, M.S., and Plemel, J.R. (2021). Regulation of microglia population dynamics throughout development, health, and disease. Glia *n/a*. *69*, 2771–2797. https://doi.org/10.1002/glia.24047.
30. Lawson, L.J., Perry, V.H., Dri, P., and Gordon, S. (1990). Heterogeneity in the distribution and morphology of microglia in the normal adult mouse brain. Neuroscience *39*, 151–170. https://doi.org/10.1016/0306-4522(90)90229-W.
31. Bruttger, J., Karram, K., Wörtge, S., Regen, T., Marini, F., Hoppmann, N., Klein, M., Blank, T., Yona, S., Wolf, Y., et al. (2015). Genetic cell ablation reveals clusters of local self-renewing microglia in the mammalian central nervous system. Immunity *43*, 92–106. https://doi.org/10.1016/j.immuni.2015.06.012.
32. Mendes, M.S., Le, L., Atlas, J., Brehm, Z., Ladron-de-Guevara, A., Matei, E., Lamantia, C., McCall, M.N., and Majewska, A.K. (2021). The role of P2Y12 in the kinetics of microglial self-renewal and maturation in the adult visual cortex in vivo. Elife *10*, e61173. https://doi.org/10.7554/eLife.61173.
33. Ratz, M., von Berlin, L., Larsson, L., Martin, M., Westholm, J.O., La Manno, G., Lundeberg, J., and Frisén, J. (2022). Clonal relations in the mouse brain revealed by single-cell and spatial transcriptomics. Nat. Neurosci. *25*, 285–294. https://doi.org/10.1038/s41593-022-01011-x.
34. Casano, A.M., Albert, M., and Peri, F. (2016). Developmental apoptosis mediates entry and positioning of microglia in the zebrafish brain. Cell Rep. *16*, 897–906. https://doi.org/10.1016/j.celrep.2016.06.033.
35. Svahn, A.J., Graeber, M.B., Ellett, F., Lieschke, G.J., Rinkwitz, S., Bennett, M.R., and Becker, T.S. (2013). Development of ramified microglia from early macrophages in the zebrafish optic tectum. Dev. Neurobiol. *73*, 60–71. https://doi.org/10.1002/dneu.22039.
36. Vollmer, J., Casares, F., and Iber, D. (2017). Growth and size control during development. Open Biol. *7*, 170190. https://doi.org/10.1098/rsob.170190.
37. Greulich, P., MacArthur, B.D., Parigini, C., and Sanchez-Garcia, R.J. (2021). Universal principles of lineage architecture and stem cell identity in renewing tissues. Development *148*. https://doi.org/10.1242/dev.194399.
38. Elmore, M.R.P., Najafi, A.R., Koike, M.A., Dagher, N.N., Spangenberg, E.E., Rice, R.A., Kitazawa, M., Matusow, B., Nguyen, H., West, B.L., and Green, K.N. (2014). Colony-stimulating factor 1 receptor signaling is necessary for microglia viability, unmasking a microglia progenitor cell in the adult brain. Neuron *82*, 380–397. https://doi.org/10.1016/j.neuron.2014.02.040.
39. Mendonsa, A.M., Na, T.-Y., and Gumbiner, B.M. (2018). E-cadherin in contact inhibition and cancer. Oncogene *37*, 4769–4780. https://doi.org/10.1038/s41388-018-0304-2.
40. Pavel, M., Renna, M., Park, S.J., Menzies, F.M., Ricketts, T., Füllgrabe, J., Ashkenazi, A., Frake, R.A., Lombarte, A.C., Bento, C.F., et al. (2018). Contact inhibition controls cell survival and proliferation via YAP/TAZ-autophagy axis. Nat. Commun. *9*, 2961. https://doi.org/10.1038/s41467-018-05388-x.

41. Tsuboi, A., Ohsawa, S., Umetsu, D., Sando, Y., Kuranaga, E., Igaki, T., and Fujimoto, K. (2018). Competition for space is controlled by apoptosis-induced change of local epithelial Topology. Curr. Biol. *28*, 2115–2128.e5. https://doi.org/10.1016/j.cub.2018.05.029.

42. Navarro, P., Gómez, M., Pizarro, A., Gamallo, C., Quintanilla, M., and Cano, A. (1991). A role for the E-cadherin cell-cell adhesion molecule during tumor progression of mouse epidermal carcinogenesis. J. Cell Biol. *115*, 517–533. https://doi.org/10.1083/jcb.115.2.517.

43. Valdivia, A., Cárdenas, A., Brenet, M., Maldonado, H., Kong, M., Díaz, J., Burridge, K., Schneider, P., San Martín, A., García-Mata, R., et al. (2020). Syndecan-4/PAR-3 signaling regulates focal adhesion dynamics in mesenchymal cells. Cell Commun. Signal. *18*, 129. https://doi.org/10.1186/s12964-020-00629-3.

44. Streichan, S.J., Hoerner, C.R., Schneidt, T., Holzer, D., and Hufnagel, L. (2014). Spatial constraints control cell proliferation in tissues. Proc. Natl. Acad. Sci. USA *111*, 5586–5591. https://doi.org/10.1073/pnas.1323016111.

45. Imai, Y., Ibata, I., Ito, D., Ohsawa, K., and Kohsaka, S. (1996). A novel gene iba1 in the major histocompatibility complex class III region encoding an EF hand protein expressed in a monocytic lineage. Biochem. Biophys. Res. Commun. *224*, 855–862.

46. Weber, K., Thomaschewski, M., Benten, D., and Fehse, B. (2012). RGB marking with lentiviral vectors for multicolor clonal cell tracking. Nat. Protoc. *7*, 839–849. https://doi.org/10.1038/nprot.2012.026.

47. Sasmono, R.T., and Williams, E. (2012). Generation and characterization of macgreen mice, the Cfs1r-EGFP transgenic mice. In Leucocytes: Methods and Protocols, R.B. Ashman, ed. (Humana Press), pp. 157–176. https://doi.org/10.1007/978-1-61779-527-5_11.

48. Muzumdar, M.D., Tasic, B., Miyamichi, K., Li, L., and Luo, L. (2007). A global double-fluorescent Cre reporter mouse. genesis *45*, 593–605. https://doi.org/10.1002/dvg.20335.

49. Baddeley, A., Rubak, E., and Turner, R. (2016). Spatial Point Patterns: Methodology and Applications with R, First Edition (CRC Press). https://doi.org/10.1201/b19708.

50. Goldmann, T., Wieghofer, P., Müller, P.F., Wolf, Y., Varol, D., Yona, S., Brendecke, S.M., Kierdorf, K., Staszewski, O., Datta, M., et al. (2013). A new type of microglia gene targeting shows TAK1 to be pivotal in CNS autoimmune inflammation. Nat. Neurosci. *16*, 1618–1626. https://doi.org/10.1038/nn.3531.

51. Egle, A., Harris, A.W., Bath, M.L., O'Reilly, L., and Cory, S. (2004). VavP-Bcl2 transgenic mice develop follicular lymphoma preceded by germinal center hyperplasia. Blood *103*, 2276–2283. https://doi.org/10.1182/blood-2003-07-2469.

52. Behringer, R., Gertsenstein, M., Nagy, K., and Nagy, A. (2014). Manipulating the Mouse Embryo: A Laboratory Manual, Fourth Edition (Cold Spring Harbor).

53. O'Koren, E.G., Yu, C., Klingeborn, M., Wong, A.Y.W., Prigge, C.L., Mathew, R., Kalnitsky, J., Msallam, R.A., Silvin, A., Kay, J.N., et al. (2019). Microglial function is distinct in different anatomical locations during Retinal homeostasis and degeneration. Immunity *50*, 723–737.e7. https://doi.org/10.1016/j.immuni.2019.02.007.

54. Åkerblom, M., Sachdeva, R., Quintino, L., Wettergren, E.E., Chapman, K.Z., Manfre, G., Lindvall, O., Lundberg, C., and Jakobsson, J. (2013). Visualization and genetic modification of resident brain microglia using lentiviral vectors regulated by microRNA-9. Nat. Commun. *4*, 1770. https://doi.org/10.1038/ncomms2801.

55. Brawek, B., Liang, Y., Savitska, D., Li, K., Fomin-Thunemann, N., Kovalchuk, Y., Zirdum, E., Jakobsson, J., and Garaschuk, O. (2017). A new approach for ratiometric in vivo calcium imaging of microglia. Sci. Rep. *7*, 6030. https://doi.org/10.1038/s41598-017-05952-3.

56. Schindelin, J., Arganda-Carreras, I., Frise, E., Kaynig, V., Longair, M., Pietzsch, T., Preibisch, S., Rueden, C., Saalfeld, S., Schmid, B., et al. (2012). Fiji: an open-source platform for biological-image analysis. Nat. Methods *9*, 676–682. https://doi.org/10.1038/nmeth.2019.

57. Smith, M. (2017). Ternary: An R Package for Creating Ternary Plots. Zenodo. https://doi.org/10.5281/zenodo.5556001.

58. Ripley, B.D. (1988). Statistical Inference for Spatial Processes (Cambridge University Press). https://doi.org/10.1017/CBO9780511624131.

59. Arnold, L. (1995). Stoyan, D.; Stoyan, H., Fractals, Random Shapes and Point Fields. Methods of Geometrical Statistics. XIV, 389 pp., Chichester etc., John Wiley & Sons 1994. ISBN 0–471–93757–6. Z. Angew. Math. Mech. *75*, 614. https://doi.org/10.1002/zamm.19950750815.

60. Gillespie, D.T. (1977). Exact stochastic simulation of coupled chemical reactions. J. Phys. Chem. A *81*, 2340–2361. https://doi.org/10.1021/j100540a008.

61. Parigini, C., and Greulich, P. (2020). Universality of clonal dynamics poses fundamental limits to identify stem cell self-renewal strategies. Elife *9*, e56532. https://doi.org/10.7554/eLife.56532.

62. Klein, A.M., Brash, D.E., Jones, P.H., and Simons, B.D. (2010). Stochastic fate of p53-mutant epidermal progenitor cells is tilted toward proliferation by UV B during preneoplasia. Proc. Natl. Acad. Sci. USA *107*, 270–275. https://doi.org/10.1073/pnas.0909738107.

STAR★METHODS

KEY RESOURCES TABLE

REAGENT or RESOURCE	SOURCE	IDENTIFIER
Antibodies		
Chicken anti-GFP	Abcam	Cat# ab13970
Rabbit anti-GFP	Santa Cruz Biotechnology	Cat# sc-8334
Goat anti-Iba1	Invitrogen	Cat# PA518488
Rabbit anti-Iba1	In-house (Covalab)	Produced in-house using peptide sequence reported in Imai et al.[45]
Rabbit anti-Olig2	Santa Cruz Biotechnology	Cat# sc-48817
Rabbit anti-PU.1	Cell Signaling Technology	Cat# 2258
Rabbit anti-PU.1	Santa Cruz Biotechnology	Cat# sc-352
Rabbit anti-Caspase 3 (cleaved)	Merck Millipore	Cat# PC679
Rabbit anti-Ki67	Abcam	Cat# ab15580
Bacterial and virus strains		
LeGO-EBFP2	Addgene[46]	Cat# 85213
LeGO-V2	Addgene[46]	Cat# 27340
LeGO-C2	Addgene[46]	Cat# 27339
Lenti-mCherry.miR-9.T	This paper, available upon request	N/A
Lenti-Venus.miR-9.T	This paper, available upon request	N/A
Lenti-mTurquoise2.miR-9.T	This paper, available upon request	N/A
Chemicals, peptides, and recombinant proteins		
Tamoxifen	Merck	Cat# T5648-1G
Experimental models: Cell lines		
N13	Cajal Institute (Spain)	N/A
Experimental models: Organisms/strains		
C57BL/6J	Harlan	N/A
c-fms EGFP	Laboratory of David Hume	Sasmono et al.[47]
Cx3cr1CreER	Jackson Laboratory	Cat# 020940
Vav-Bcl2	Laboratory of Andreas Strasser	Askew et al.[12]
Rosa26mT/mG	Laboratory of Salah Elias	Muzumdar et al.[48]
Oligonucleotides		
Primer for Rosa^{mTmG} Genotyping (Mutant forward 5'-TAGAGCTTGCGGAACCCTTC-3')	This paper	N/A
Software and algorithms		
Prism 9	GraphPad	https://www.graphpad.com/
ImageJ	ImageJ	https://imagej.nih.gov/ij/
RStudio	Rstudio	https://www.rstudio.com/
SpatStat	Baddeley et al.[49]	https://cran.r-project.org/web/packages/spatstat/index.html
Ternary	Martin R. Smith	https://cran.r-project.org/web/packages/Ternary/vignettes/Ternary.html
Inkscape		https://inkscape.org/

RESOURCE AVAILABILITY

Lead contact

Further information and requests for resources and reagents should be directed to and will be fulfilled by the lead contact, Diego Gomez-Nicola (d.gomez-nicola@soton.ac.uk).

Materials availability

This study did not generate new unique reagents.

Data and code availability

- Primary data is available from the lead contact upon request.
- This paper does not report original code.
- Any additional information required to reanalyze the data reported in this paper is available from the lead contact upon request.

EXPERIMENTAL MODEL AND SUBJECT DETAILS

Animals

All mice were maintained according to Home Office regulations and experiments were approved by a local ethical review committee in accordance with the UK animals (Scientific Procedures) Act (1986), and conducted under relevant personal and project licenses. All mice used were bred on a C57BL/6 background. C57BL/6 and *c-fms* EGFP mice[47] (hereafter referred to as Macgreen) were used for time course analysis of microglia throughout embryonic and postnatal life. For lineage tracing experiments, homozygous Rosa$^{mT/mG}$[48] males were crossed with homozygous Cx3cr1^{CreER}[50] female mice to generate Rosa$^{mT/mG}$ x Cx3cr1^{CreER} mice (hereafter referred to as Cx3cr1^{CreER}; Rosa$^{mT/mG}$). *Vav-Bcl2* mice[51] were used as a model of myeloid-specific apoptosis prevention, as previously described for microglia.[12] C57BL/6 mice were used for all *in vivo* experiments involving stereotaxic injection of vectors for RGB marking.

For developmentally timed experiments, trios were set up late in the afternoon. Following this, female mice were checked daily for a vaginal plug. The day on which the plug was identified was noted as embryonic day 0.5, or E0.5, estimating the time of copulation to be 12 h after initial pairing based on the light-dark cycle and mating habits of mice.[52] Female mice that had a vagina plug were separated from males. Single litters arising from the same dam were analysed at each timepoint.

Cell lines

The N13 cell line of microglial cells was used for the characterisation of RGB marking using LeGO vectors.[25,26,46] The cells were cultured according to manufacturer's guidelines in Dulbecco's Modified Eagle's Medium (D-MEM) that was supplemented with 10% fetal bovine serum (FBS) and Penicillin-Streptomycin (all ThermoFisher Scientific).

METHOD DETAILS

Induction of cre-dependent sparse labelling of microglia with EGFP

Cx3cr1^{CreER}; Rosa$^{mT/mG}$ mice were used for sparsely labelling microglia with an EGFP tag. The Rosa$^{mT/mG}$ transgene contains the fluorescent proteins tdTomato and EGFP under the Rosa26 promoter.[48,50] For sparse labelling microglia with EGFP during development, we first prepared stocks of 20 mg/ml and 10 mg/ml of TAM and 4-OH TAM by solubilising in ethanol (100%) and dissolving in corn oil (Sigma-Aldrich) (1 hr; 60°C). TAM and 4-OH TAM were sonicated using a bench top vortex until completely solubilised. The stock solution of TAM was supplemented with 10 mg of progesterone to offset the reported off-target effects of TAM during pregnancy.[53] Using low doses of TAM allowed labelling of a very small percentage of microglia arising during early embryonic development. Pregnant Cx3cr1^{CreER} dams that had been mated with male Rosa$^{mT/mG}$ mice received an i.p. injection of TAM (200 mg/kg, 62.5 mg/kg or 12.5 mg/kg) on either E9.5 or E10.5. Dams were weighed and closely monitored following injection for any signs of sickness behaviour or resorption of pregnancy. For optimisation purposes, the subsequent offspring were analysed 24 hours post injection (hpi) in order to estimate the initial rate of EGFP labelling in CX3CR1^{+} cells. Following optimisation, a time course was established following i.p. injection of TAM (12.5 mg/kg) to pregnant dams at E10.5 with subsequent analysis of sparse labelled microglia in Cx3cr1^{CreER}; Rosa$^{mT/mG}$ offspring at E11.5, E16.5 and P30 (from a single litter for each timepoint).

Multicolour fate mapping with RGB vectors

Production and use of VSVG-SFFV-RGB vectors

RGB marking of cells can be achieved by transduction with a combination of LeGO vectors encoding a red, green and blue fluorescent protein[26] hereby referred to as RGB vectors. LeGO vectors are 3rd generation, self-inactivating lentiviral vectors derived from HIV-1, containing all necessary cis-active elements for packaging, reverse transcription and integration into the host cell genome and are therefore suitable for the stable and long-term labelling of mammalian cells with fluorescent proteins.[26] Due to the random nature of the transduction with the tree RGB vectors, target cells display a unique colour hue resulting from a stochastic mixture of the three basic colours, that is inherited by all daughter cells and thus is suitable for clonal analysis.[26] Moreover, RGB vectors can be engineered for cell specificity by use of cell-specific promoters and can be used for *in vitro* and *in vivo* studies.[25]

For *in vitro* based RGB marking of N13 cells, SFFV-RGB vectors were used, as the strong and ubiquitous spleen focus forming virus (SFFV) promotor allows stable expression in glial cells.[25] Packaging with the envelope protein from vesicular stomatitis virus (VSVG) leads to high vector titers and a broad tropism of the viral particles. The titers were further increased by centrifugation at 8,000 g and

4°C overnight. We made available all LeGO vectors used here through Addgene.org: LeGO-EBFP2 (Addgene #85213), LeGO-V2 (Addgene #27340) and LeGO-C2 (Addgene #27339). A combination of SFFV-RGB vectors encoding; enhanced blue fluorescent protein (EBFP2) (titer per ml = 3.39 x 10^9), Venus (titer per ml = 7.86 x 10^9) and mCherry (titer per ml =3.39 x 10^9) were used at an equimolar concentration. N13 cells were initially seeded at low densities (between 10 and 100 cells per well) in order to try and achieve clonal colonies over time. After 24 h, the cells were transduced with 10 μL of this SFFV-RGB vector mix and incubated for a further 24 h. The media was changed in order to remove the RGB vectors and the cells were maintained for 5 more days before fixation and analysis. To analyse the potential colour spread of the RGB-marked cells, a second experimental setup was used where N13 cells were initially transfected with 150 μl of the above SFFV-RGB vector mix while in T75 flasks. The flasks of N13 cells were split 24 h after transfection and subsequently seeded at low densities (1000 or 100 cells per well) in order to induce the growth of clonal colonies. After 6 days, cells were fixed with 2% PFA and washed with PBS before confocal analysis of RGB marked colonies.

Production of Lenti-RGB.miR-9.T vectors

For producing the Lenti-RGB.miR-9.T vectors, we modified the parent construct (LV.GFP.miR-9.T)[54], which incorporates four target sites (5′-TCATACAGCTAGATAACCAAAG-3′) for microRNA-9 (miR-9) downstream of GFP, thus causing the degradation of the fluorescent protein-encoding messenger RNA or silencing of the construct's expression in cells expressing miR-9. Because unlike the other brain cells of neuroectodermal origin (e.g., neurons, astrocytes and oligodendrocytes) microglia lack miR-9 expression, this approach favors selective labeling of microglia.[54,55] Lenti-RGB.miR-9.T vectors were generated by replacing GFP with either mCherry, Venus, or mTurquoise2. Cell-free supernatants containing viral particles were produced by transient transfection of HEK293T packaging cells with the lentiviral construct and helper plasmids (psPAX2 and pMD2G) as described previously.[55] After 48 h the virus-containing culture supernatant was collected, filtered through a 0.45 μm pore-sized filter and concentrated by centrifugation at 27,000 rpm for 2 h at 4 °C by using Thermofisher WX Ultra80 centrifuge (Waltham, MA, USA). Pellets were re-suspended in sterile PBS and stored at -80 °C. Viral solutions with a titre higher than 10^8 colony forming units/ml were used in this study.

In vivo *transduction of microglia with RGB vectors*

SFFV-RGB vectors and Lenti-RGB.miR-9.T vectors (mir-RGB vectors) were used for *in vivo* tracing of microglia. In order to induce multicolour labelling of microglia during postnatal development, SFFV-RGB vectors encoding the fluorescent proteins mCherry (red), Venus (green) and enhanced blue fluorescent protein (EBFP)(blue) were stereotaxically injected (1 μl) at an equimolar concentration into the right brain hemisphere of postnatal *C57BL/6* pups (n=3) at P0. The injected mice were closely monitored for signs of sickness behaviour and subsequently culled after 21 days for histological analysis. To increase the specificity of transduction in microglia, we used the mir-RGB vectors under the control of the widely expressed phosphoglycerate kinase (PGK) promoter.[54] For experiments using mir-RGB vectors, postnatal *C57BL/6* pups (n=5) received an ipsilateral injection at P0 to the right hemisphere with 1μl of an equimolar mix of mir-RGB vectors encoding the fluorescent proteins mCherry (red), Venus (green) and mTurquoise (blue). A control group (n=2) did not receive any injection. Following injection, the mice were closely monitored for signs of sickness behaviour. Mice were culled 30 days following injection for histological analysis.

Immunohistochemistry

Sagittal or coronal brain sections were cut at a thickness of either 80 μm or 30 μm from paraformaldehyde-fixed brains using a vibratome as described previously.[27] Whole embryos were embedded in paraffin wax and sectioned using a microtome. Embryos were cut parasagittal to the sagittal midline at a thickness of 10μm. In total 3 series were collected per embryo with 2 sections per representative area consistent with anatomical guidelines from the Allen brain atlas for the developing mouse brain. Sections for brightfield microscopy were initially incubated with Dako dual enzyme block to quench endogenous peroxidase and alkaline phosphatase (AP) activity (Agilent Technologies) (15 min; RT) and then washed with PBST0.1%. Wax embedded sections contained additional dewaxing (60°C oven for 1h and xylene), rehydration (sequential rehydration in ethanol; 100% to dH2O) and antigen retrieval (boiled in citrate buffer for 15 min) steps prior to quenching. To prevent unspecific binding of primary and secondary antibodies, sections were incubated with a blocking solution made in PBST0.2 (0.2% Tween20) and containing 5% bovine serum albumin (BSA) and 5% of the appropriate animal serum of the secondary antibody host animal (1 hr; RT). Sections were incubated with primary antibodies (ON; 4°C) that were appropriately diluted in blocking solution: chicken anti-GFP (Abcam; ab13970; 1:500), rabbit anti-GFP (Santa Cruz Biotechnology; sc-8334; 1:500), rabbit anti-Iba1 (Wako; 1:500), goat anti-Iba1 (Invitrogen; PA518488; 1:500), rabbit anti-Olig2 (Santa Cruz Biotechnology; sc-48817; 1:500), rabbit anti-PU.1 (Cell Signalling Technology; 2258; 1:500), rabbit anti-PU.1 (Santa Cruz Biotechnology; sc-352; 1:500), rabbit anti-Caspase3 (Merck Millipore; PC679; 1:50) or rabbit anti-Ki67 (Abcam; ab15580; 1:500). Sections were washed and then incubated with appropriately diluted biotinylated secondary antibodies (Vector) or Alexa-488, Alexa-568 and Alexa-647 fluorescent secondary antibodies (Invitrogen). For immunofluorescence, sections were incubated with the nuclear counterstain DAPI (1:200) in PB (10 min; RT) and then washed with PB (3 x 5 min; RT) and finally mounted on gelatinised slides and coverslipped with Mowiol DABCO (Sigma). For brightfield microscopy, sections were incubated with the avidin-biotin complex (ABC) kit and visualised with horse-radish peroxidase substrate diaminobenzidine (DAB) (2.5%) and/or BCIP/NBT kit (Vector) according to the manufacturer's instructions. Methyl green (Vector) was used as a counterstain. Sections were mounted on gelatinized slides and coverslipped with Mowiol DABCO or DPX (Sigma).

Image acquisition and analysis

Fluorescent signal was detected and visualised using a Leica DM5000 B microscope or a Leica SP8 confocal system. 3-D confocal stacks were acquired from tissues transduced with RGB vectors using the laser scanning function of the Leica SP8 confocal microscope with a 20x 0.75NA objective at a resolution of 1.3 pixels per μm. Z stacks were acquired at 1.14 μm per step in the Z plane from either 35 μm or 80 μm tissue sections. Confocal tile scanning of whole sagittal tissue sections was carried out using the Leica SP8 confocal microscope using the spiral scan function in Leica LAS-X software program. Brightfield images of DAB and AP staining were obtained using a Leica DM5000 B microscope or an Olympus VS110 slide scanner at a resolution of 2.9 pixels per μm.

Images were analysed using Fiji analysis software.[56] The CellCounter plugin was used to record the number of cells and their spatial coordinates (XY) on at least 3 sections per animal. For each antigenic marker, the cell density (cells/mm^2) was calculated as the overall cell number divided by the area of the ROI (mm^2) (n=3 sections/mouse). For analysis of double positive cells, the deconvolution tool was used for separation of the chromogenic markers, DAB and AP. Delineated boundaries were saved as an ROI file and the spatial coordinates of each boundary were exported using the ROI manager tool in Fiji.

Analysis of microglia transduced with RGB vectors

Fiji was used for analysis of RGB fluorescent colour from multicolour labelling experiments in N13 cells and postnatal mice that had been transduced with RGB vectors. An automated macro was developed for analysis of RGB colour from *in vitro* experiments. Briefly, the cell somas of fluorescently labelled microglia were delineated from maximum projection of confocal stacks. For *in vitro* analysis, the colour histogram tool was used to calculate the mean intensity in the red, green and blue channel for microglia cell soma from RGB images. For *in vivo* experiments, a manual analysis was used in order to reduce any noise and avoid artefacts. Images acquired from *in vivo* experiments were converted from composite to RGB images and the channels were split into corresponding red, green and blue images which were displayed in greyscale. The average intensity in the red, green and blue channel for each microglia soma was calculated by measuring the mean grey value for each image. The resultant RGB colour space was mapped onto ternary graphs as a percentage of colour intensity using the Ternary Package in RStudio.[57] For *in vitro* analysis of RGB colour spread within clonal clusters, the distance (arbitrary units (AU)) was measured between two of the furthest points, *a* and *b*, on the ternary plot using the distance formula for the *X*, *Y* and *Z* coordinates of each point:

$$AU = \sqrt{(X_a - X_b)^2 + (Y_a - Y_b)^2 + (Z_a - Z_b)^2}$$

Spatial analysis using SpatStat

The SpatStat package in RStudio was used for analysis of the spatial distribution of cells.[49] The two-dimensional coordinates (XY) for 2-D images and three-dimensional coordinates (XYZ) for 3-D stacks were saved as .csv files and imported as a dataset into RStudio. Point patterns were generated using the coordinates of each cell and the coordinates delineating the boundary of the area of interest. For spatial analysis of two different cell types from the same image (i.e., PU.1$^+$ cells and Caspase3$^+$ cells), a subsequent column defining the cell type was included. For analysis of multiple cell types, the 'mark' function was used to define the cell type. The point patterns were converted to density heat maps based on a kernel bandwidth of 25 or 50 μm (command 'Density' in SpatStat) in order to represent the spatial distribution of cells.

Nearest neighbor analysis

The average nearest neighbour distance was computed using SpatStat (command 'nndist') which will compute the nearest distance from a cell to the next in a point pattern. The resultant vector of values was exported as .csv files and used to compute the average nearest neighbour distance. For calculation of the nearest neighbour values from the 1st to 100th neighbouring cell, the range of 1-100th neighbour was specified and returned as the mean distance. The resultant vectors of values were exported as .csv files.

2-D Ripley's K spatial analysis

Statistical spatial analysis was carried out using Ripley's K function (command 'Kest' in SpatStat) in order to characterise the spatial distribution of microglia over a given radius. The K function of a stationary point process*X* was defined so that lambda *K*(*r*) equals the expected number of additional random points within a distance *r* of a typical random point of *X*. Here lambda is the intensity of the process, i.e. the expected number of points of *X* per unit area. The K function was determined by the second order moment properties of *X*. In order to make inferences about the spatial distribution, the estimate of *K* for the observed spatial points was compared to the true value of *K*for a completely random (Poisson) point process, which is:

$$K(r) = \pi r^2$$

Deviations between the observed and Poisson K curves suggested spatial clustering or spatial regularity. The estimates of K(r) are of the form:

$$Kest(r) = (a / (n * (n - 1))) * sum[i,j]\, I(d[i,j] <= r)\, e[i,j])$$

where*a* refers to the area of the window, *n* is the number of data points, and the sum is taken over all ordered pairs of points *i* and *j* in X. Here *d*[*i*,*j*] is the distance between the two points, and *I*(*d*[*i*,*j*] <= *r*) is the indicator that equals 1 if the distance is less than or equal to *r*. The term *e*[*i*,*j*] is the edge correction weight which is applied to reduce bias.[58] The correction implemented here is Ripley's isotropic correction used for rectangular and polygonal windows.[58]

Points were assumed to be randomly distributed when the observed *K*(*r*) was equal to the theoretical *K*(*r*). Points were considered as uniformly distributed or dispersed when the observed *K*(*r*) was less than the theoretical *K*(*r*). Conversely, when the observed *K*(*r*) was greater than the theoretical *K*(*r*), the points were considered clustered. Observed *K*(*r*) and theoretical *K*(*r*) values were assessed over the first quartile of each K function. Observed *K*(*r*) and theoretical *K*(*r*) values were also calculated as averages over the entire K function. Subtraction of the theoretical *K*(*r*) from the observed *K*(*r*) was used for normalisation across different point patterns. The L-function (*L*(*r*)) was used for spatial analysis of microglia from *Vav-Bcl2* mice. Briefly, the L-function is a square-root transformation of the K-function, producing a linear value whereby L(r)=r under complete spatial randomness.

3-D Ripley's K spatial analysis

For confocal stacks, Ripley's K function was estimated from 3-D patterns (command 'K3est' in SpatStat). For three-dimensional stationary point processes *Phi*, the three-dimensional *K*function is

$$K3(r) = \left(\frac{1}{lamda}\right) E(N(Phi, x, r) \mid x \; in \; Phi$$

where*lambda* is the intensity of the process (the expected number of points per unit volume) and *N*(*Phi*,*x*,*r*) is the number of points of *Phi*, other than *x* itself, which fall within a distance *r* of *x*. This is the three-dimensional generalisation of Ripley's *K* function for two-dimensional point processes.

The three-dimensional point pattern X is assumed to be a partial realisation of a stationary point process*Phi*. The distance between each pair of distinct points was computed. The observed cumulative distribution function of these values, with appropriate edge corrections, was renormalised to give the estimate of *K3*(*r*). The edge correction implemented here was the three-dimensional counterpart of Ripley's isotropic correction.

Marked connect function of multitype point patterns

The mark connection function *p*[*A*,*B*](*r*) was used as a measure of the spatial dependence between two cell types of a process *X* at distance *r* apart. The mark connect function *p*[*A*,*B*](*r*) is defined as the conditional probability, given that there is a point of the process at a location *u* and another point of the process at a location *v* separated by a distance ||*u*-*v*|| = *r*, that the first point is of type *A* and the second point is of type B.[59] If the marks attached to the points of *X* are independent and identically distributed, then *p*[*A*,*B*](*r*) = *p*[*A*]*p*[*B*] where *p*[*A*] denotes the probability that a point is of type *A* and *p*[*B*] denotes the probability that a point is of type *B*. Values larger than this, *p*[*A*,*B*](*r*) > *p*[*A*]*p*[*B*], indicate positive association between the two types, while smaller values indicate negative association. For analysis of spatial dependence across animals, the probability of an independent association *p*[*A*]*p*[*B*] was subtracted from the calculated mark connect function *p*[*A*,*B*](*r*). Therefore, any positive values for, *p*[*A*,*B*](*r*) > *p*[*A*]*p*[*B*] indicate a dependence between the points *A* and *B*. Conversely any negative values are indicative of an independent spatial association.

Modelling microglial fate dynamics

The model for proliferation and fate of microglia distinguishes between proliferating cells (P), which will divide at some point, and non-proliferating cells (N), which have exited cell cycle or are about to do so. When proliferating cells divide, each daughter cell can either go on to proliferate (remaining in state P) or exit cell cycle (attaining state N). Hence, upon division, the following fates are possible:

$$P \xrightarrow{\lambda} \left\{ \begin{array}{c} P + P \; with \; probability \; r(1+\delta) \\ P + N \; with \; probability \; 1 - 2r) \\ N + N \; with \; probability \; r(1 - \delta) \end{array} \right\}, N \xrightarrow{d} \varnothing$$

where λ is the division rate of P-cells (here, rates are generally defined as the inverse of the mean time between events). The cell fate probabilities are parametrised by r, the proportion of symmetric divisions, and δ, the bias towards proliferation. Furthermore, we will consider the scenario that P-cells may remain initially quiescent and activate proliferation at a certain time point t_0, which we refer to as model version 2. We also consider the situation where some clones have higher proliferative activity than others, i.e. where λ, r, d or δ variate between clones, (i.e. the proliferative potential is inherited to daughter-P-cells). We implement cell divisions as a Markov process, i.e. cell divisions occur independently of each other at constant stochastic rate. We simulate this model by a Gillespie algorithm.[60] We note that while the Markov property does not reflect the realistic distributions of individual cell division times, the clonal statistics produced by any cell cycle distribution with a finite variance converge quickly – after a few cell divisions – to the same clonal distribution (this is an instance of a more generalised central limit theorem.[61] Hence a Markov model has the same predictions as a model with more realistic cell cycle time distributions, and we chose the Markov model for its simplicity.

To test the model versions on the NND (nearest neighbour distance) data we used an analytical approach to predict the NND as function of clone size. The NND can be estimated by the average distance, a, between neighbouring cells in a clone, which is related to the cell density of a clone as $a \propto \rho^{-1/3}$, with cell density $\rho = \frac{n}{V}$, where *n* is the number of cells in a clone and *V* the typical 'volume' of the clone. *V* is initially the volume of one cell and grows while the clone spreads at rate $\nu = \frac{dn}{dt}$ when cells of the clone and other,

interspersed cells in the background (belonging to other clones) divide, which occurs at the same rate as the net proliferation rate averaged over all clones, $\frac{dV}{dt} = \bar{\nu}$. In model version 3, when microglia start proliferating at the same time but with different proliferation rates ν, V is on average the same for all clones (since the average $\bar{\nu}$ is taken over all clones), and therefore $\rho = \frac{n}{V} \propto n$, thus $a \propto n^{-1/3}$. On the other hand, for model version 2, when clones start to proliferate at different times, but the same proliferation rate, $\nu = \bar{\nu}$, then for each clone both n and V grow with the same rate, namely $\bar{\nu}$, and therefore $\rho = \frac{n}{V}$ is constant. Hence, also a does not vary with n. For the latter estimate, we assume that the differences in clone sizes are mainly due to differences in the start time of proliferation rather than stochastic fluctuations (as has been argued in detail in[62]).

QUANTIFICATION AND STATISTICAL ANALYSIS

All data were analysed using the statistical package Graph Pad Prism 9 (GraphPad Software, Inc.). When assumptions of normality were reached, statistical analyses were performed using either a Student's t-test when comparing between two groups, or a two-way analysis of variance (ANOVA) when comparing across two variables, followed by Tukey's or Bonferroni's post-hoc tests for multiple comparisons. Where assumptions of normality were not reached, either the Kruskal-Wallis or Mann Whitney test were applied. Linear regression and Pearson's correlation test were performed for correlation analysis. A p value of less than 0.05 was considered statistically significant. Data are expressed as mean ± standard error of the mean (SEM).